ChemEngineering

MDPI

*Article*

# Numerical Investigation into Effects of Gas Sparger and Horizontal Baffles on Hydrodynamics of Flat Bubble Column

**Masroor Abro [1,2,*], Imran Nazir Unar [2,3], Junaid Korai [4], Abdul Qudoos [5], Sikandar Almani [2], Abdul Qadeer Laghari [2], Liang Yu [6] and Abdul Sattar Jatoi [7]**

1 Beijing Key Laboratory of Membrane Science & Technology, College of Chemical Engineering, Beijing University of Chemical Technology, Beijing 100029, China
2 Process Simulation and Modeling Research Group, Chemical Engineering Department, Mehran University of Engineering and Technology, Jamshoro 76062, Pakistan; inunar@illinois.edu (I.N.U.); sikander.almani@faculty.muet.edu.pk (S.A.); abdul.qadeer@admin.muet.edu.pk (A.Q.L.)
3 Nuclear and Plasma Radiological Engineering Department, Grainger College of Engineering University of Illinois Urbana-Champaign, Urbana, IL 61801, USA
4 Departament d'Enginyeria Química, Universitat Rovira i Virgili, Avinguda Països Catalans 26, 43007 Tarragona, Spain; junaidghaffar.korai@urv.cat
5 Centre of Carbon Capture, Utilisation and Storage (CCCUS), Institute of Sustainable Energy and Resources (ISER), Universiti Teknologi Petronas, Bandar Seri Iskandar 32610, Malaysia; abdul_22009731@utp.edu.my
6 Agricultural and Biological Engineering, School of Engineering and Technology, Kentucky State University, Frankfort, KY 40601, USA; liang.yu@kysu.edu
7 Chemical Engineering Department, Dawood University of Engineering and Technology, Karachi 74800, Pakistan; abdul.sattar@duet.edu.pk
* Correspondence: masroor.abro@faculty.muet.edu.pk; Tel./Fax: +92-313-8822800

## Abstract

Computational fluid dynamics (CFD) was used to investigate influence of different gas sparger configurations and the presence of horizontal baffles on hydrodynamic characteristics in a flat bubble column. CFD results of time-averaged local and global gas holdup, liquid axial velocity, and Sauter mean diameter were experimentally validated. Subsequently, the validated CFD model was extended to investigate the effects of different gas sparger configurations, i.e., $S_1$, $S_3$, $S_4$, $S_5$, $S_8$, and $S_{72}$, and baffles arrangements, i.e., Config-A and Config-B on overall hydrodynamics at different superficial gas velocities ($U_g$ = 0.0014 m/s and 0.0073 m/s). CFD results demonstrated significant influence of both sparger and $U_g$. Gas holdup and interfacial area increased with smaller, more numerous sparger openings, such that $S_{72}$ achieved 1.55 times higher holdup and 2 higher interfacial area than that of $S_1$. Spargers with fewer and larger openings induced stronger turbulence, which intensified early breakup and coalescence and broadened the bubble size distribution. Results revealed that spargers with many small openings ($S_{72}$) produced the narrowest distribution, retaining a high fraction of bubbles of initial size (5 mm), whereas spargers with fewer larger openings ($S_1$) generated broader distributions with significant coalescence, especially at higher $U_g$. The inclusion of baffles enhanced liquid circulation and gas–liquid mixing and contact. However, intensified turbulence below each baffle significantly increased coalescence, producing larger bubbles and resulting in only marginal changes in interfacial area despite increased gas holdup.

**Keywords:** bubble column; CFD modeling; bubble size distribution; gas sparger; baffles

check for updates

Academic Editor: Roumiana Petrova Stateva

Received: 17 October 2025
Revised: 30 November 2025
Accepted: 9 December 2025
Published: 12 December 2025

**Citation:** Abro, M.; Unar, I.N.; Korai, J.; Qudoos, A.; Almani, S.; Laghari, A.Q.; Yu, L.; Jatoi, A.S. Numerical Investigation into Effects of Gas Sparger and Horizontal Baffles on Hydrodynamics of Flat Bubble Column. *ChemEngineering* **2025**, *9*, 144. https://doi.org/10.3390/chemengineering9060144

**Copyright:** © 2025 by the authors. Licensee MDPI, Basel, Switzerland. This article is an open access article distributed under the terms and conditions of the Creative Commons Attribution (CC BY) license (https://creativecommons.org/licenses/by/4.0/).

## 1. Introduction

Bubble columns are widely used in industrial chemical, petrochemical, biochemical, pharmaceutical, mineral, and physical separation processes [1,2]. Due to several advantageous features, such as high heat and mass transfer coefficients, interfacial area and phase fluxes, low operating cost, simple construction, and easy maintenance, these are attractive for industrial applications [3–5]. A critical aspect in the design and scale-up of bubble columns is investigation of hydrodynamics, which governs their overall performance [6,7]. Thus, strong knowledge of key hydrodynamic parameters (gas holdup, interfacial area, bubble size distribution, and liquid velocity) is essential [8,9]. However, hydrodynamics of bubble columns are inherently complex, being strongly influenced by geometry, gas sparger, operating conditions, and presence of internals [10,11]. For instance, the development of a flow regime in bubble column can significantly be affected by gas sparger configuration as well as by incorporating the internals in bubble columns [12].

Previous studies have highlighted the role of gas spargers in influencing the hydrodynamic behavior of bubble columns. Bhole et al. [13] compared two different spargers and found different hydrodynamic behaviors. Similarly, Gemello et al. [14] experimentally investigated bubble columns with two different spargers and reported different profiles of local gas holdup and Sauter mean diameter. McClure et al. [15] demonstrated that type of sparger strongly affects local gas holdup and liquid velocity. Marchini et al. [16] measured the coefficient of gas dispersion in bubble columns with different gas spargers. Similarly, one can refer to the previous literature on the inclusion of certain internals such as vertical tubes, horizontal baffles, or sieved trays in the bubble column, wherein their substantial effect on hydrodynamic characteristics was observed [12,17,18]. The addition of horizontal baffles/trays in bubble columns can result in a sufficient degree of mixing between phases without the need for any moving/rotating parts, ultimately intensifying the mass/heat transfer rates. Alvaré et al. [19] investigated a sectionalized bubble column consisting of perforated trays and reported an increase in overall gas holdup compared with columns without trays. In baffled and packed bubble columns, Xia et al. [18] obtained significant improvement in phase mixing as a result of multiple vortexes formation. Liu et al. [20] reported that the internals in a bubble column can significantly impact the hydrodynamics and transport process. Collectively, these studies demonstrate the critical role of sparger design and internals; however, their combined effect in flat bubble columns remains insufficiently explored.

To address this challenge, computational fluid dynamics (CFD) has been increasingly adopted as a complementary tool. CFD offers significant advantages over experimental techniques by providing detailed insights into underlying physical mechanisms and supporting the efficient design and scale-up of multiphase contactors [21,22]. Previously, CFD has been extensively applied to predict bubble column hydrodynamics, demonstrating its potential use in design and scale-up [23–25]. Liang et al. [26] used CFD to predict the effect of two gas spargers with different opening areas on bubble size distribution (BSD) and local gas holdup profiles. Guo et al. [27] simulated the role of vertical internals on the hydrodynamics of bubble columns with the help of CFD. A widely reported approach to simulate the multiphase scenario in bubble columns is Euler–Euler (E-E) [24,28]. It is widely applied to most multiphase flows over a wide range of dispersed phase void fractions. It can effectively predict the dynamics by assuming a mean bubble size only in a uniform flow regime that is characterized by weak bubble–bubble interactions and less turbulence in the external field [7]. However, practically, the size of the bubble formed at a sparger is unstable and undergoes temporal and spatial variation, especially for turbulent flow regimes. Under these conditions, a wider range of BSD exists, which is a significant parameter strongly affecting the overall gas holdup, gas–liquid interfacial area, as well as

the flow regime. To capture the effects of BSD on multiphase hydrodynamic characteristics, population balance modeling (PBM) is coupled with the Euler–Euler model [29,30]. Coupling CFD with PBM improves predictive accuracy, even in the bubbly flow regime reported in previous studies [31–33]. Bannari et al. [34] demonstrated improved accuracy in model validation with the aid of PBM compared to using mean bubble size only. Nevertheless, most CFD-PBM studies have been limited to cylindrical bubble columns, while flat geometries with sparger-internal combinations remain largely unexplored.

Flat bubble columns, a main classification of multiphase contacting devices, have been widely used to characterize multiphase flow behavior at a lab scale [5,35,36]. Their controllable operating conditions, compatibility with advanced experimental techniques, and simpler CFD implementation make them attractive for fundamental investigations [37]. Observations from flat bubble columns also provide valuable insights for design and scale-up of industrial systems. These aspects have been explored using advanced experimental techniques such as laser doppler anemometry (LDA) [38], radioactive particle tracking (RPT) [39], and particle image velocimetry (PIV) [40]. Prior studies have mainly focused on interfacial forces and PBM methods [36,41], the influence of superficial gas velocity, and liquid height on dynamic flow properties [42,43]. However, little attention has been given to the combined effects of sparger configuration and internals in flat bubble columns. Developing such understanding is essential for advancing both laboratory-scale investigations and industrial-scale designs.

This work develops a CFD-PBM framework for an air–water flat bubble column that incorporates a comprehensive set of interfacial closures, i.e., drag, lift, virtual mass, and wall lubrication, together with coalescence-breakage kernels. Unlike most previous CFD-PBM studies, which typically examine a single sparger geometry or focus solely on either sparger effects or internal structures, the present model is applied systematically to six spargers with identical total area but different numbers, sizes, and arrangements of openings, as well as two baffled configurations. This enables a unified investigation of how sparger design and horizontal baffles jointly influence gas holdup, liquid circulation, bubble size distribution, and interfacial area in flat columns, which are scarcely explored in existing literature. The model is experimentally validated for gas holdup, axial velocity, and Sauter mean diameter, and the validated framework is then used to generalize hydrodynamic trends across all geometries. These developments highlight both the predictive strength and the broader applicability of the proposed CFD-PBM model for understanding and optimizing multiphase behavior in bubble columns.

## 2. Model Equations

In this study, a multiphase scenario is modeled in the E-E framework, wherein each phase is considered as an interpenetrating continuum, and their movement is taken in a Eulerian reference frame. It does not encounter discrete bubble tracking. The phase interaction is achieved through various interfacial forces. For each phase, the conservation equations are converged separately.

### *2.1. Continuity Equations*

The continuity equations for the Eulerian multiphase model are given below.

The equation of continuity for continuous phase is given as follows [44]:

$$\frac{\partial}{\partial t}\left(\alpha_p \rho_p\right) + \nabla\left(\alpha_p \rho_p v_p\right) = 0 \quad (1)$$

The dispersed phase enters the column with a mean particle size, which is highly unstable because both the coalescence and breakage phenomena result in the birth and

death of particles, occurring due to turbulence, varying bubble rise velocity and phase interface, and so on [7,34]. Using PBM, the bubble coalescence breakage mechanisms are studied to accurately predict BSD. Several numerical methods of PBM, such as the multi class/bins method and moment method, have been employed [45]. In this work, the homogeneous discrete method (also known as the bins method) is implemented in which a population of bubbles is divided on a pivotal grid using the fixed pivot approach proposed by Kumar et al. [46]. All the bubbles are assumed to be moving with the same velocity, which is simply the gas phase velocity. This method is advantageous in terms of predicting the particle size distribution directly; however, it is more computationally expensive than the moment-based method.

The continuity equation of dispersed phase is written for the volume fraction of each $i^{th}$ bin as follows:

$$\frac{\partial}{\partial t}(\alpha_q \rho_q f_i) + \nabla(\alpha_q \rho_q v_q f_i) = S_i \tag{2}$$

In Equation (2), $S_i$ is a source term which considers the birth and death terms of bubbles belonging to bin $i$ due to coalescence and breakage. When assuming no interphase mass transfer and uniform bubble size, $S_i$ is taken as zero. It is mathematically defined as follows [47,48]:

$$S_i = \rho_g (B_i^c - D_i^c + B_i^{br} - D_i^{br}) \tag{3}$$

where $i$ ranges from 1 to N:

$$B_i^c = \left( \frac{1}{2} \int_0^v a(v - v', v') n(v - v') n(v') dv' \right) \tag{4}$$

$$D_i^c = \left( n(v) \int_0^\infty a(v, v') n(v') dv' \right) \tag{5}$$

Bubble coalescence in turbulent flow occurs when two bubbles collide, trapping a thin liquid film, which drains and ruptures once it reaches a critical thickness, allowing bubbles to merge; otherwise, they rebound. Coalescence is mainly driven by shear, turbulence, and buoyancy. This study employed the Luo coalescence kernel [49], which assumes coalescence due to turbulent fluctuation only. The coalescence rate $r_c$ is the product of coalescence efficiency and frequency of collision:

$$r_c = \omega_c (v_i, v_j) P_c (v_i, v_j) \tag{6}$$

Collision frequency $\omega_c (v, v')$ is calculated as function of the characteristic velocity and collision cross-sectional area.

$$\omega_c (v, v') = \left[ \frac{\pi}{4} (d_i + d_j)^2 n_i n_j \right] \left( \overline{u}_i^2 + \overline{u}_j^2 \right)^{1/3} \tag{7}$$

$d_i$ and $d_j$ are the colliding bubbles' diameters, $\overline{u}$ is the characteristic velocity of their collision, and $n_i$ and $n_j$ are their number densities, respectively.

$$\overline{u}_i = \sqrt{2} (\varepsilon d_i)^{1/3} \tag{8}$$

The coalescence efficiency $P_c(v, v')$ is given as follows:

$$P_c(v, v') = exp \left\{ -C_l \frac{\sqrt{\left[ 0.75(1 + \vartheta_{ij}{}^2)(1 + \vartheta_{ij}{}^3) \right] We_{ij}}}{\sqrt{\left( \frac{\rho_q}{\rho_p} + 0.5 \right)} (1 + \vartheta_{ij})^3} \right\} \tag{9}$$

where $\vartheta_{ij} = d_i/d_j$, and $We_{ij}$ represents the Weber number, which is equal to $\frac{\rho_p d_i(\overline{u})^2}{\sigma}$.

$B_i^{br}$ is the birth term of smaller bubbles due to the breakage of larger bubbles:

$$B_i^{br} = \int_v^{\infty} m(v')b(v')p(v,v')n(v')dv' \tag{10}$$

$p(v,v')$ accounts for the probability density function of daughter bubbles, and $m(v')$ is the mean number of daughter bubbles generated from breakage of a parent bubble of volume $v'$. The death term of bubbles due to breakage $D_i^{br}$ is as follows:

$$D_i^{br} = b(v)n(v) \tag{11}$$

$b(v)$ represents the breakage frequency of bubbles of volume $v$. The rate of bubble breakage was calculated using the model proposed by Lehr et al. [50]. This model assumes that bubble breakage is induced by eddies of varying length scales. Binary breakage occurs when eddies smaller than the bubble diameter impact its surface, while larger eddies only transport bubbles. The eddy length scale must exceed the diameter of the resulting daughter bubbles, as expressed by the following relation:

$$d_d \leq \gamma \leq d_{b,br} \tag{12}$$

where $d_d$ is the diameter of the bubble formed after breakage, $\gamma$ is the length scale of the eddy, and $d_{b,br}$ is the diameter of the bubble undergoing breakage. Mathematically, Lehr et al. [50] define the breakage rate $r_{br}$ as follows:

$$r_{br} = \frac{1.19\sigma}{\rho_p \varepsilon^{1/3} d^{7/3} {f_{bv}}^{1/3}} \int_{\xi_{min}}^{1} \frac{(1+\xi)^2}{\xi^{11/3}} exp\left(-\frac{2\sigma We_{crit}}{\rho_p \varepsilon^{\frac{2}{3}} d^{\frac{5}{3}} {f_{bv}}^{\frac{1}{3}}}\right) \tag{13}$$

Both of these kernels are sensitive to turbulence parameters; thus, any turbulence model error maps into PBM.

In Equation (2), $f_i$ denotes the individual bin size fraction and is given as follows [35]:

$$f_i = \frac{\alpha_i}{\alpha_q} \tag{14}$$

And

$$\sum_i f_i = 1 \tag{15}$$

where $\alpha_i$ is the bin volume fraction, related to the number density as follows:

$$\alpha_i = n_i V_i \tag{16}$$

$n_i$ ($m^{-3}$) is the bubble number density or number of bubbles from bin $i$ per unit volume.

$V_i$ is the bubble volume belonging to bin $i$, which can be expressed as follows:

$$V_i = K_v d_i^3 \tag{17}$$

$K_v$ is a volume coefficient to 0.5235988, and $d_i$ is the bubble diameter from bin $i$.

The total sum of $\alpha_i$ gives the volume fraction occupied by the dispersed phase.

$$\alpha_q = \sum_i \alpha_i \tag{18}$$

Equations (15)–(18) were obtained from [34].

The mean bubble size throughout the fluid domain is represented by Sauter mean diameter ($d_{32}$), which is very significant towards the momentum enclosures; thus, any change in $d_{32}$ also results in a change in overall flow dynamics. It is computed as follows:

$$d_{32} = \frac{1}{\sum_i \left(\frac{f_i}{d_i}\right)} \tag{19}$$

*2.2. Momentum Equations*

Based on the assumption of a common velocity field shared by all the bubbles, the conservation equation of momentum is given as follows:

$$\begin{aligned} &\frac{\partial}{\partial t}(\alpha_p \rho_p \boldsymbol{v}_p) + \nabla(\alpha_p \rho_p \, \boldsymbol{v}_p \boldsymbol{v}_p) \\ &\quad = -\alpha_p \nabla p + \nabla\left[\alpha_p \mu_p^{eff}\left(\nabla \boldsymbol{v}_p + \nabla \boldsymbol{v}_p^T\right) + \alpha_p\left(\lambda_p - \frac{3}{2}\mu_p^{eff}\right)\nabla \boldsymbol{v}_p \overline{\overline{I}}\right] + \alpha_p \rho_p \vec{g} + \boldsymbol{F_q} \end{aligned} \tag{20}$$

where $p$ is the pressure shared by both phases, and $\mu_p^{eff}$ represents the effective viscosity of the continuous phase. The standard $k$-$\varepsilon$ turbulence model was employed to estimate the effective viscosity, assuming negligible effect of molecular viscosity [51]:

$$\mu_p^{eff} = \mu_p^l + \mu_p^t + \mu_b^t \tag{21}$$

where $\mu_p^t$ is given as follows [52]:

$$\mu_p^t = \frac{C_\mu \rho_p k^2}{\varepsilon} \tag{22}$$

The transport equation of turbulent kinetic energy ($k$) and turbulence dissipation rate ($\varepsilon$) are as follows [53]:

$$\frac{\partial}{\partial t}(\alpha_p \rho_p k_p) + \nabla(\alpha_p \rho_p \, \boldsymbol{v}_p k_p) = \nabla\left(\alpha_p\left(\mu + \frac{\mu_p^t}{\sigma_k}\right)\nabla k_p\right) + \alpha_p(G_k - \rho_p \rho \varepsilon_p) \tag{23}$$

$$\frac{\partial}{\partial t}(\alpha_p \rho_p \varepsilon_p) + \nabla(\alpha_p \rho_p \, \boldsymbol{v}_p \varepsilon_p) = \nabla\left(\alpha_p\left(\mu + \frac{\mu_p^t}{\sigma_\varepsilon}\right)\nabla \varepsilon_p\right) + \alpha_p \frac{\varepsilon_p}{k_p}(C_1 G_k - C_2 \rho_p \rho \varepsilon_p) \tag{24}$$

$\mu_b^t$ is computed as proposed by Sato et al. [54]:

$$\mu_b^t = C_{\mu,b} \alpha_q \rho_p d \left|\boldsymbol{v}_p - \boldsymbol{v}_q\right| \tag{25}$$

The default values of model constants were used.

The standard $k$-$\varepsilon$ turbulence model was selected in this study due to its robustness, low computational cost, and simple algorithm [55]. It has been successfully applied in CFD-PBM coupled setups within lower ranges of superficial gas velocity, achieving satisfactory agreement with experimental results [56].

Interfacial Closures

In Equation (20), $\boldsymbol{F_q}$ represents the total interfacial momentum source term governing interphase interactions. Effective momentum transfer between continuous and dispersed phases needs suitable models due to their complex coupling [57]. In this study, drag, virtual mass or added mass, lift, and wall lubrication forces were incorporated to ensure accurate interphase coupling. The total interfacial force is expressed as follows:

$$\boldsymbol{F_q} = -\boldsymbol{F_p} = \boldsymbol{F_D} + \boldsymbol{F_L} + \boldsymbol{F_{VM}} + \boldsymbol{F_W} \tag{26}$$

where $\boldsymbol{F_D}$ is termed as drag force, which has been observed as most significant towards the flow phenomena in bubble columns compared to other interfacial forces [58,59]. The momentum exchange between phases resulting from drag force can be expressed as follows:

$$\boldsymbol{F_D} = \frac{3}{4} C_D \frac{\alpha_q \rho_p}{d} |\boldsymbol{v}_q - \boldsymbol{v}_p| (\boldsymbol{v}_q - \boldsymbol{v}_p) \tag{27}$$

where $C_D$ is calculated using the model proposed by Grace [60], which is suitable for low-viscous flows with different shaped bubbles. However, likewise, other drag models, i.e., Ishii and Zuber [61] and Tomiyama et al. [62], need to be corrected with a swarm factor for particular conditions [63]:

$$C_D = \frac{4}{3} \frac{gd}{U_t^2} \frac{(\rho_q - \rho_p)}{\rho_p} \tag{28}$$

where

$$U_t = \frac{\mu_p}{\rho_p d_{32}} Mo^{-0.149} (J - 0.857) \tag{29}$$

$J$ is an empirical function of the Morton ($Mo$) and Eötvös ($Eo$) numbers and can be computed as follows:

$$J = \begin{cases} 0.94H^{0.757} & 2 < H \leq 59.3 \\ 3.42H^{0.441} & H > 59.3 \end{cases} \tag{30}$$

$$H = \frac{4}{3} EoMo^{-0.149} \left( \frac{\mu_p}{\mu_{ref}} \right)^{-0.14} \tag{31}$$

$\mu_{ref}$ is equal to 0.0009 Pa·s.

$\boldsymbol{F_L}$ is the lift force, which is a transverse force experienced by dispersed phase particles when they move in rotational flow [64]. Due to the velocity gradient in the flow field [65], it is especially significant in setting the flow direction. By adding the lift force with drag, oscillation of the bubble plume can be captured more effectively, which sometimes becomes hard with drag only [35]. It can be calculated as defined by Žun [66].

$$\boldsymbol{F_L} = -C_L \rho_p \alpha_q (\boldsymbol{v}_q - \boldsymbol{v}_p) \times (\nabla \times \boldsymbol{v}_p) \tag{32}$$

$C_L$ is the lift coefficient, which is important due to its negative or positive value [67]. In the current setup, the lift force model of Legendre et al. [68] has been used, which is computed as follows:

$$C_L = \sqrt{\left\{ \frac{6}{\pi^2} (Re_b Sr)^{-0.5} \frac{2.55}{\left(1 + 0.2 \frac{Re_b}{Sr}\right)^{1.5}} \right\}^2 + \left\{ \frac{1}{2} \frac{1 + 16 Re_b^{-1}}{1 + 29 Re_b^{-1}} \right\}^2} \tag{33}$$

where $Re_b$ denotes the bubble Reynolds number and $Sr = \frac{Re_\omega}{Re_b}$.

Virtual mass force $\boldsymbol{F_{VM}}$ accounts for the acceleration of liquid due to the relative acceleration of surrounding bubbles [69]. When PBM is implemented in the CFD setup, $\boldsymbol{F_{VM}}$ in combination with lift force improves the accuracy in the near wall as well as the central region of the column [70]. The mathematical definition of $\boldsymbol{F_{VM}}$ is given as follows:

$$\boldsymbol{F_{VM}} = C_{VM} \alpha_q \rho_p \left( \frac{d_q \boldsymbol{v}_q}{dt} - \frac{d_p \boldsymbol{v}_p}{dt} \right) \tag{34}$$

In Equation (34), $C_{VM}$ is the virtual mass coefficient, which is equal to 0.5 in this study.

The wall lubrication force $\boldsymbol{F_W}$ arises when bubbles approach the wall; it accounts for displacement of bubbles away from the wall.

$$\boldsymbol{F_W} = -C_W \alpha_q \rho_p \left| \boldsymbol{v}_q - \boldsymbol{v}_p \right|^2 \vec{n}_W \tag{35}$$

$\vec{n}_W$ is the unit vector pointing towards the center of wall. Presently, $C_W$, proposed by Hosokawa et al. [71], is used:

$$C_W = max\left( \frac{7}{Re^{1.9}}, 0.0217Eo \right) \tag{36}$$

## 3. Numerical Settings, Fluid Domain, and Model Assumptions

A flat bubble column 0.2 m in width, 0.45 m in height (height of quiescent liquid), and 0.05 m in depth, similar to experimental studies [38,39,42,72], was used. It consists of a gas sparger at bottom comprising of eight holes, each 0.8 mm in diameter, arranged in a rectangular array, as depicted in Figure 1a. For the simulation, following past studies [34,41], the actual gas sparger was replaced with a rectangle of area covering the gas openings; this replacement can be reasonable while using the E-E framework [73]. The fluid domain was physically discretized into structured but non-uniformly distributed mesh with minimum orthogonal quality equal to 1 and maximum skewness of 0, using GAMBIT 2.4.6. At the initial stage, three grid sizes, i.e., Fine, Medium, and Coarse (details are given in Figure 1b–d and Table 1), were selected for the basic geometry to perform grid sensitivity analysis.

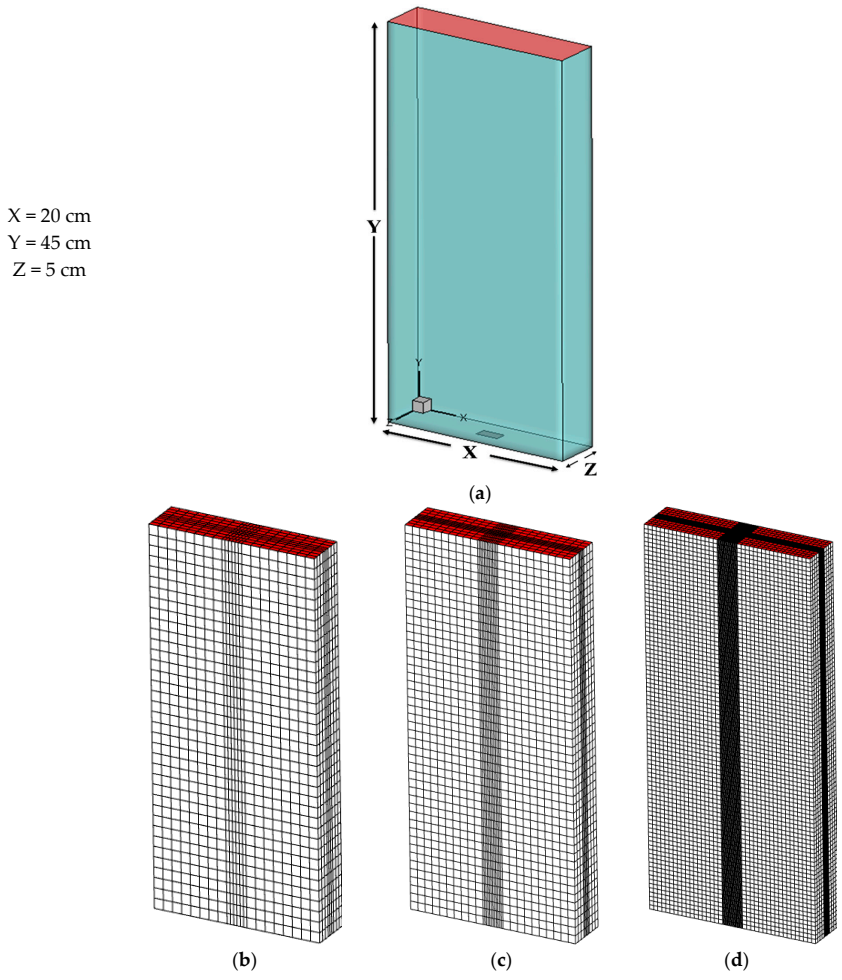


**Figure 1.** (**a**) 3D physical domain of actual bubble column, (**b**) coarse grid, (**c**) medium grid size, and (**d**) find grid size.

**Table 1.** Description of different grid sizes.

| | Coarse | Medium | Fine |
|---|---|---|---|
| Sparger | 6 × 3 | 12 × 5 | 24 × 12 |
| Full domain | 14 × 37 × 6 | 20 × 47 × 6 | 36 × 90 × 8 |
| Total elements | 7326 | 16,544 | 108,000 |

For further study, five more gas spargers different in number, size, and arrangement of gas openings but same in overall opening area (2.88 $cm^2$) were used. A schematic representation of all spargers is presented in Figure 2.

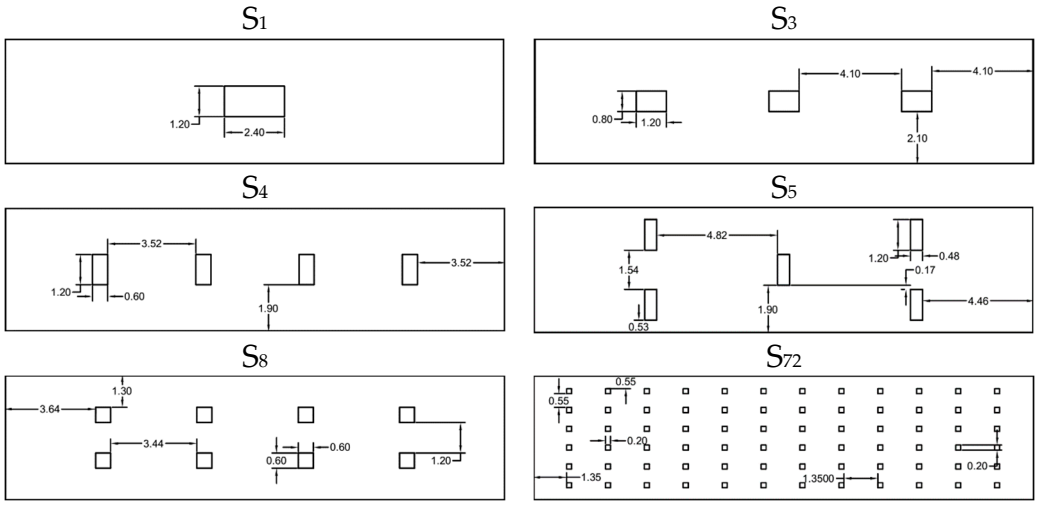


**Figure 2.** Details of spargers used in the simulation (the dimensions are given in cm).

Moreover, the internal structure of the column was modified by inserting horizontal baffles in two different arrangements; the details are presented in Section 4.2.2.

All the simulations were performed using ANSYS Fluent 16.0. The semi-batch column consisted of water as a quiescent phase, and air was sparged with uniform bubble size via the velocity inlet at the bottom. Table 2 summarizes the initial and boundary conditions and numerical settings.

**Table 2.** Initial and boundary conditions and numerical settings.

| | |
|---|---|
| Inlet | Velocity inlet<br>$U_g$ = 0.0014 m/s and 0.0073 m/s<br>$k$ and $\varepsilon$ were set to an initial value of 1<br>Population balance variables were specified as mono-dispersed BSD |
| Outlet | Pressure outlet (set to atmospheric pressure) |
| Simulation type | Transient |
| Time step size ($\Delta t$) | 0.005 s–0.01 s (fixed) |
| Gravity | $-9.81$ m/$s^2$ (Y-direction) |
| Wall | Stationary<br>No-slip condition was used for both phases |
| Pressure–velocity coupling | Phase-coupled SIMPLE |

**Table 2.** *Cont.*

| | |
|---|---|
| Discretization Schemes<br>Momentum, volume fraction<br>Turbulent kinetic energy and dissipation rate and air bin | First-order upwind |
| Transient formulation | First-order implicit |
| Under relaxation factors | Default values for each |
| Continuous phase | Water<br>$\rho = 998$ Kg/m$^3$<br>$\mu = 0.001$ Pa·s<br>$\sigma = 0.0732$ N/m |
| Dispersed phase | Air<br>$\rho = 1.225$ Kg/m$^3$<br>$\mu = 1.78 \times 10^{-5}$ Pa·s |

As mentioned in Section 2.1, population balance was modeled using the bins/class method, which requires prior information of bubble size to be assigned for each bin. Table 3 summarizes the bubble size ranging from 1 mm to 22 mm divided into 11 bins, which are sufficient to capture the BSD under the given operating conditions and geometric specifications. Buwa et al. [72] measured a mean bubble size of 5 mm under these operating conditions. Also, using the correlation proposed by Wilkinson [74], the mean bubble size was predicted as 5 mm under the same conditions. Therefore, an inlet bubble size of 5 mm was assumed at the inlet boundary by defining the fraction of bin 6 as equal to 1.

**Table 3.** Bubble size distribution in bins.

| Bin index | 1 | 2 | 3 | 4 | 5 | 6 | 7 | 8 | 9 | 10 | 11 |
|---|---|---|---|---|---|---|---|---|---|---|---|
| Bubble size (mm) | 1.0 | 1.48 | 2.0 | 2.7 | 3.65 | 5.0 | 6.67 | 9.0 | 12.1 | 16.4 | 22 |

*Model Assumptions*

- Clean surface of bubbles is assumed, without any surfactants or impurities.
- The flow is assumed to exhibit isotropic turbulence.
- Turbulent dispersion force is not considered here.
- Bubble–bubble collisions are assumed to be dominated by turbulence.
- All the bubbles rise at the same velocity, which is the gas velocity.

## 4. Results and Discussion

### *4.1. Grid Sensitivity Analysis and Model Validation*

Grid size of a geometry is an important factor, since different grid sized geometries could produce different results. Hence, it is very important to perform grid sensitivity analysis in CFD modeling and simulation to investigate the optimum grid size for achieving accurate results at acceptable computational cost. For this purpose, the grid sensitivity was performed at low $U_g$. As illustrated in Figure 3a, the time-averaged water axial velocity showed negligible variation with grid refinement. Similarly, in Figure 3b, overall gas holdup and global $d_{32}$ exhibited minute variation, particularly from medium mesh to fine mesh, confirming that the numerical results are grid-independent. Based on these results, the medium grid size was selected for actual geometry. For geometries with other spargers, the medium grid size was applied at both the sparger and other domain to maintain consistency across simulations.

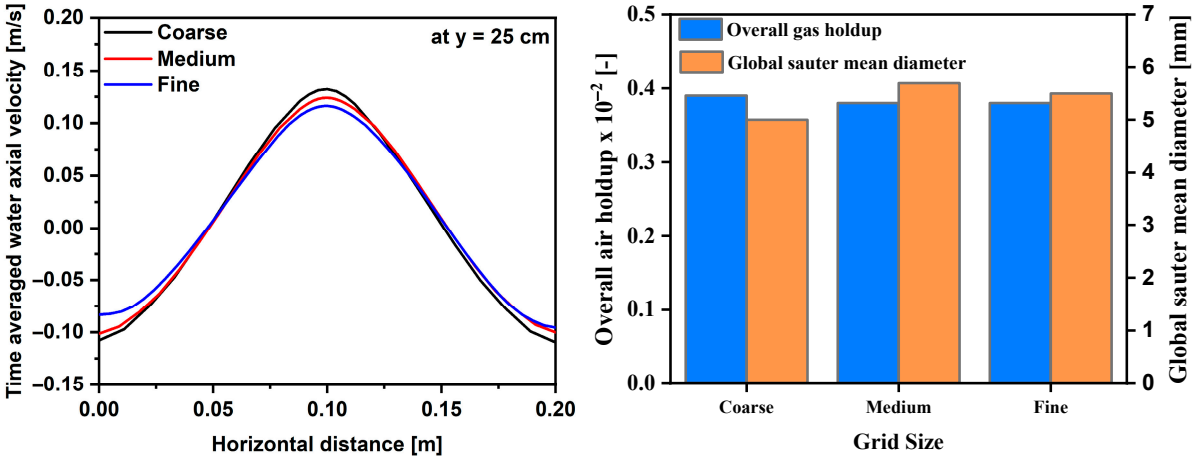


**Figure 3.** Grid sensitivity analysis at $U_g$ = 0.0014 m/s: (**a**) time-averaged water axial velocity and (**b**) overall gas holdup and global $d_{32}$.

For validating the present CFD model, time-averaged water axial velocity measured by LDA [38] and RPT [39] and time-averaged gas holdup through conductivity probes [42,72] were used. For the details of experimental procedure and conditions, the above-mentioned studies can be referred. The simulations were performed at $U_g$ of 0.0014 m/s 0.0073 m/s and 0.00833 m/s, as used in above experimental studies. The time-averaged radial profiles of water axial velocity at two different axial positions, i.e., 25 cm and 37 cm, and gas holdup at 37 cm and are compared in Figure 4. Figure 4a–d show satisfactory agreement between CFD predictions and experimental data at both axial positions under low and high $U_g$. However, an overprediction of downward water velocity by CFD is likely associated with stronger recirculation induced by bubble–liquid interactions at 25 cm (Figure 4a). At this axial level, the plume is center-dominant, causing a "cooling tower mode" characterized by strong downward flow in the vicinity of the walls and upward flow in the central region. With increasing height, the plume spreads progressively in the radial directions and weakens the recirculation near the wall, as well as the axial velocity in the center (Figure 4b). The near-wall deviation (Figure 4a) could be due to (i) imperfect time-averaging of CFD and (ii) difference the between simulated and actual gas sparger. Nevertheless, overall agreement between CFD and the experiment was satisfactory, with a maximum standard deviation of 0.015.

Also, Figure 4e,f depict a reasonable match between experimental and CFD values of local gas holdup. However, in Figure 4f, discrepancy between the simulated and experimental result of local gas holdup at high $U_g$ could be attributed to different plume oscillation, since the simulated sparger differs from the actual one.

To further validate the model over other conditions of $U_g$, simulations were performed in the range of 0.0024 m/s to 0.0213 m/s, similar to the experimental conditions of Díaz et al. [35]. In Figure 5, overall gas holdup obtained through CFD is compared with those of the experimental values of Díaz et al. [35] and the theoretical values predicted by Hughmark [75] correlation. This correlation is based on the experimental data obtained over a wide range of column dimensions, liquid properties, and $U_g$. As depicted, the CFD results are found to be in remarkable quantitative agreement with both of these, revealing the accuracy of the present CFD model, with standard deviations ranging from 0.04 to 0.44.

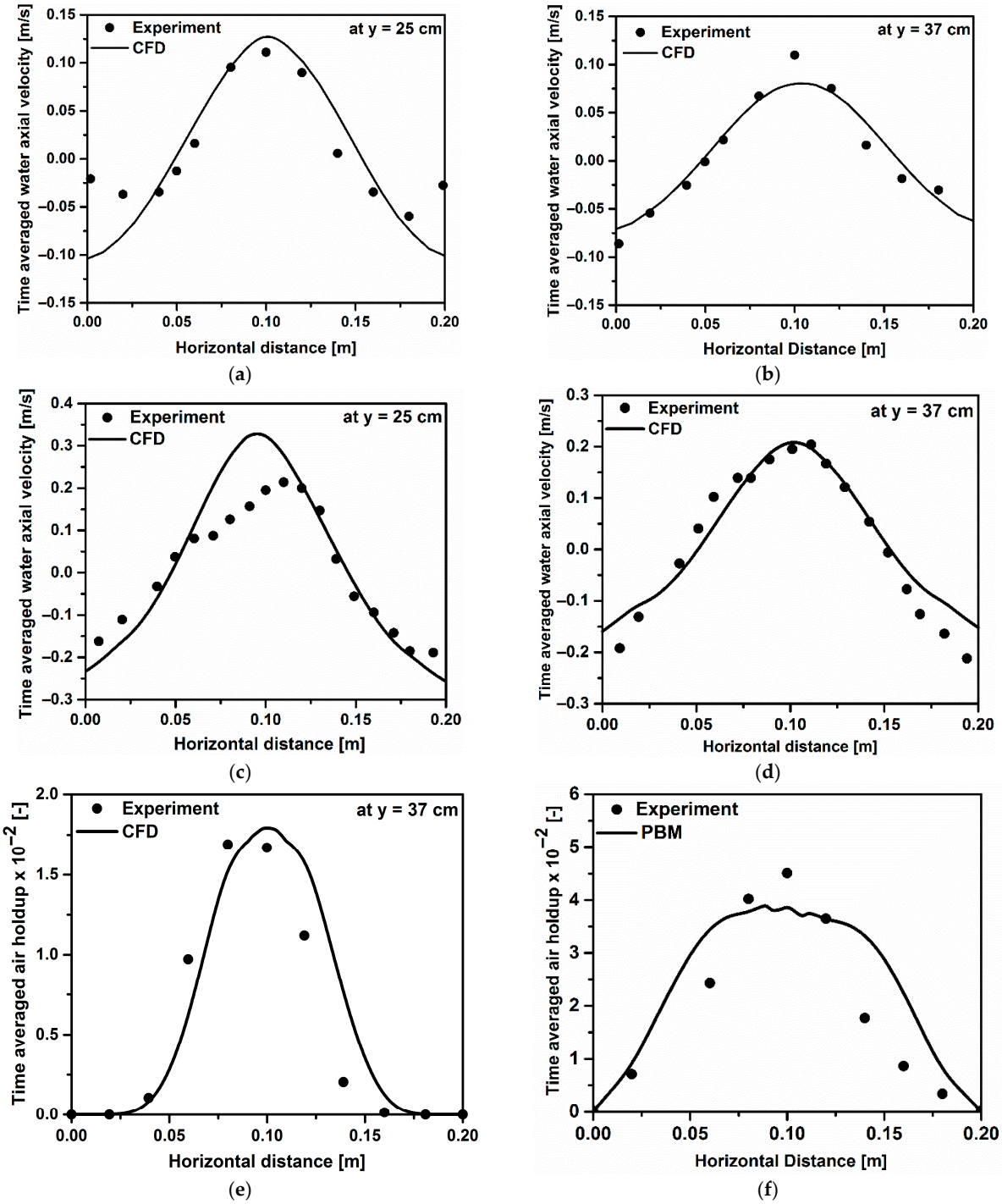


**Figure 4.** Comparison of CFD results with experimental measurements: (**a**,**b**) time-averaged water axial velocity at $U_g$ = 0.0014 m/s with Pfleger et al. [38], (**c**,**d**) time-averaged water axial velocity at $U_g$ = 0.00833 m/s with Upadhyay et al. [39], (**e**) time-averaged air holdup at $U_g$ = 0.0014 m/s with Buwa et al. [72], and (**f**) time-averaged air holdup at $U_g$ = 0.0073 m/s with Buwa et al. [42].

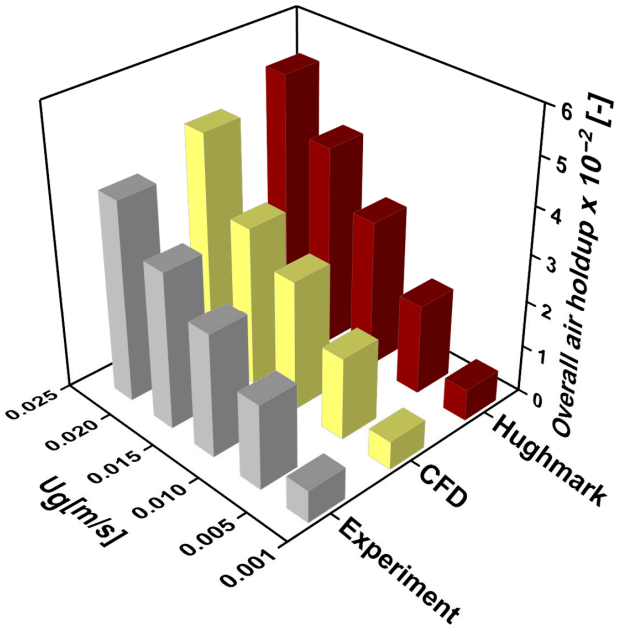


**Figure 5.** Comparison of CFD results with experimental measurement by Díaz et al. [35] and Hughmark [75] correlation at different $U_g$.

### *4.2. Simulation Results*

#### 4.2.1. Effect of Gas Sparger

Six types of spargers were used in this study; in each, the gas openings were arranged in a rectangular array. A schematic description of the spargers is given in Figure 2. The simulations were conducted at $U_g$ values of 0.0014 m/s and 0.0073 m/s.

Figure 6 illustrates contour plots of time-averaged gas holdup discerning the bubble plume trajectories for all spargers on a vertical sectional plane at high and low $U_g$ values. Obviously, the position and number of gas openings have a key role in the generation of flow patterns, as the gas entering the bubble column is responsible for driving the liquid phase. As shown in Figure 6, the gas phase entered the column via the sparger in the form of rising plumes, which were equal to number of gas openings. The plumes were perceivable in the lower region, where these seemed to oscillate and gather; the amplitude of their oscillation was high at high $U_g$ values. With increasing column height, the plumes were turned into a uniform sheet of dispersed bubbles, spread over the cross-section of the column, gradually at low $U_g$ and sharply at high $U_g$. This reveals that $U_g$ had obvious effects on both the magnitude and pattern of the gas holdup distribution. Moreover, the bubbles were dispersed uniformly over the entire cross-section at high $U_g$ values. At higher $U_g$, for $S_1$, $S_3$, $S_4$, and $S_8$, some gas phase packets detached from the plumes and were found in the vicinity of the walls, which could be assumed as gas bubbles trapped by the liquid circulation. For sparger $S_5$, the gas holdup near the walls was nearly zero in the region above the sparger; however, there was a central plume originating from bottom to top. This behavior exactly reflects the position of gas openings in the spargers. Highly uniform gas dispersion was induced by sparger $S_{72}$, with bubble plumes distinguishable just above the sparger, and uniformity increased with the number of gas openings. In all cases, the gas phase was dispersed symmetrically with respect to the vertical central line. It is noted that relatively higher gas holdup values were exhibited by $S_1$, $S_3$, $S_4$ in the middle plane due to the orientation of the gas openings on the horizontal central line. In other cases, the position of the gas openings was slightly displaced, resulting in low gas holdup.

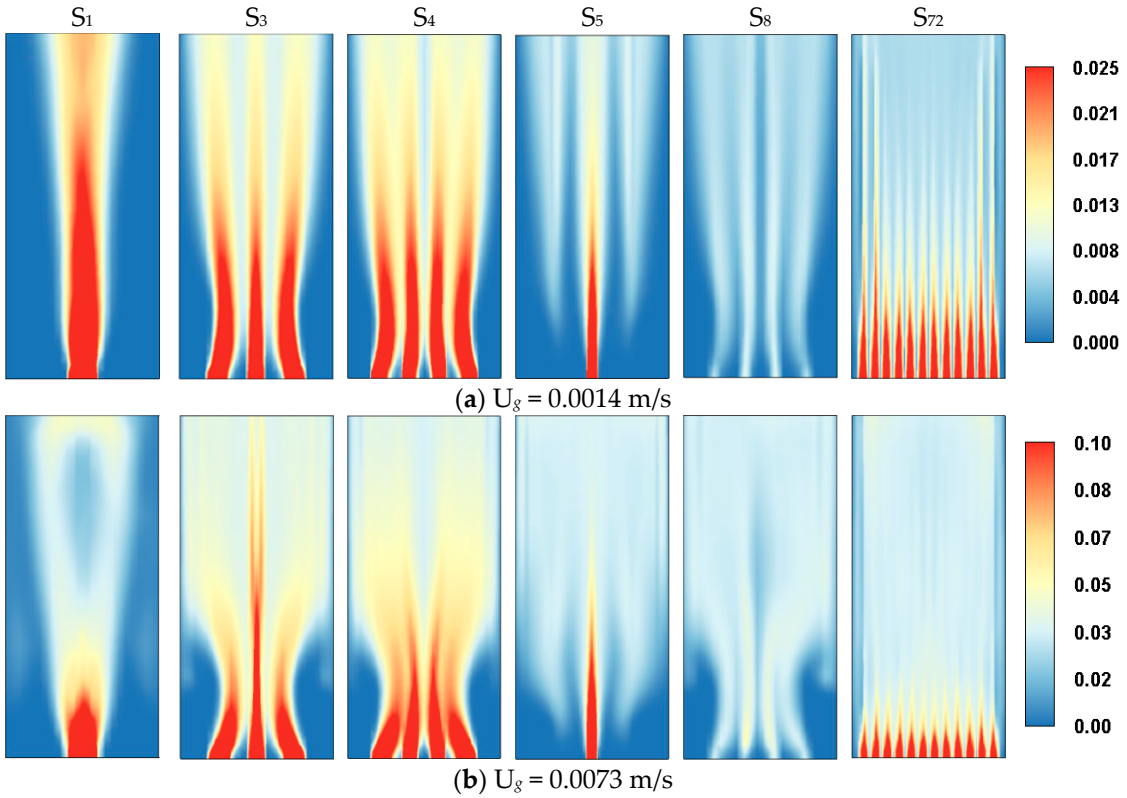


**Figure 6.** Time-averaged gas holdup distribution for different gas spargers in a vertical sectional plane under (**a**) $U_g$ = 0.0014 m/s and (**b**) $U_g$ = 0.0073 m/s. The color contours illustrate the spatial variation in local gas holdup, where red regions represent higher gas concentrations near the sparger outlets.

In this study, PBM was coupled with CFD to study the BSD. Before investigating the BSD, the present CFD results of $d_{32}$ were verified with the experimental results of Díaz et al. [35] at five different $U_g$ values in the range of 0.0024 to 0.0213 m/s. In this range, bubble breakage and coalescence phenomena are significant where the turbulence flow regime may exist. Following the experiments, a 5 mm bubble diameter was set as the mean value at the inlet boundary at each $U_g$. Moreover, Wilkinson's data [74] was also used to predict the mean bubble size, and it was obtained in the range of 4.7 mm to 4.95 mm closer to experimentally stated values under the above conditions. The global $d_{32}$ from the simulation was calculated using Equation (19). Figure 7 shows that the CFD results of global $d_{32}$ are satisfactorily agreeing with experimental measurements, especially at low $U_g$ values, indicating the accuracy of the present CFD model. At lower $U_g$, the increase in $d_{32}$ with increasing $U_g$ shows the predominance of coalescence over breakage until a maximum value is achieved. With further increases in $U_g$, a slight decrease in $d_{32}$ is observed, indicating the occurrence of breakage phenomena. The standard deviation between experimental measurement and CFD results was obtained in the range of 0.17 to 0.5, demonstrating the effectiveness of the present CFD model for the bubble column across a variety of operating conditions and possibly geometric specifications.

Figure 8 depicts the effects of the gas sparger on local $d_{32}$ in cross-sectional plane of a bubble column at 22.5 cm, which is exactly the middle height of the column. This location was selected to equally consider the effects of the gas sparger and outlet. The bubble size was larger at the locations of gas openings for low and high $U_g$ values. This was due to upward flow of dense bubble plumes with higher number density, leading to significant bubble coalescence. At low $U_g$, bubbles were uniformly distributed within a narrow size range, with coalescence being the dominant phenomenon, whereas at high $U_g$, the bubble size range increased due to enhanced coalescence and bubble breakup. Sparger $S_{72}$ showed

the highest uniformity of BSD. As observed, in some cases, small bubbles (<5 mm) were also found in the corners. This is likely due to the increase in liquid circulation along the walls/corners leading to bubble breakage with increasing $U_g$. At high $U_g$, a significant rise in the bubble concentration encouraged their coalescing behavior and ultimately caused the expansion of large bubbles in the region. These results indicate that the effect of sparger on local $d_{32}$ was noticeable at the column's middle height. Furthermore, by increasing the number of gas openings, the uniformity in the BSD was also increased.

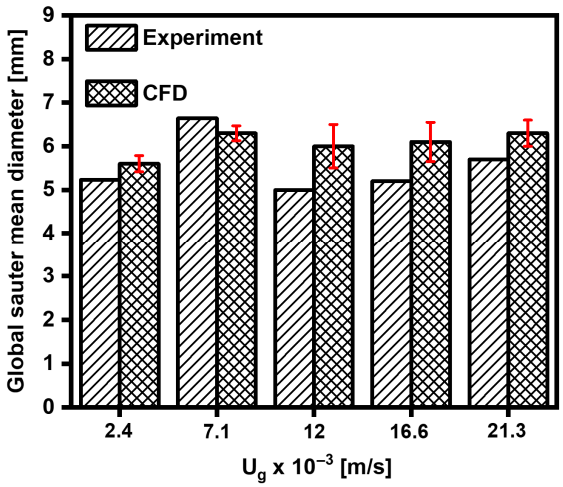


**Figure 7.** CFD prediction of global $d_{32}$ vs. experimental measurements by Díaz et al. [35] at different $U_g$ values.

Evaluation of bin size fractional distribution provides direct measurement of bubble breakage and coalescence. The $U_g$ values selected in this study fall within the uniform flow regime, where the turbulence is low and the coalescence dominates the breakage. The effect of $U_g$ and sparger on global BSD is captured through simulation and depicted in Figure 9. For clarity, bubbles in bins 1–5 are classified as small, while those in bins 7–11 are considered large. For all spargers, the maximum fraction was occupied by the bubbles of mean size (5 mm) except of $S_1$ at high $U_g$. The relative contribution of mean-sized bubbles increased in the order $S_1 < S_3 < S_4 < S_5 < S_8 < S_{72}$.

The effect of sparger on BSD was more pronounced at low $U_g$, where $S_1$ produced a distinctly non-uniform distribution. With increasing numbers of openings (and decreasing size), the BSD gradually became more uniform, reflecting reduced bubble–bubble interactions and, consequently, limited coalescence and breakage. In contrast, high $U_g$ widened the BSD by increasing both small and large bubble fractions. This effect was particularly evident in the large bubble range, owing to higher collision frequencies that enhanced coalescence, and this trend is consistent with earlier studies [26,76].

For spargers $S_4$–$S_8$, only minor differences in BSD were observed at both velocities, suggesting comparable breakage–coalescence dynamics. In contrast, $S_{72}$ exhibited unique behavior; at low $U_g$, the BSD was nearly uniform, while at high $U_g$, the fraction of large bubbles extended up to bin 9. The turbulence fields shown in Figure 10 reveal that $S_{72}$ generated the lowest values of turbulent kinetic energy ($k$) and turbulence dissipation rate ($\varepsilon$) among all spargers, owing to the uniform distribution of the gas flow into 72 low-momentum microjets, rising at relatively low velocity. Reduced turbulence generated by $S_{72}$ compared to $S_1$ is consistent with the trend previously reported in [77]. The reduced turbulence minimizes shear-induced bubble deformation and turbulent-driven breakage, consistent with predictions from the Lehr breakage kernel [50], while the low k also diminishes collision intensities, limiting coalescence in accordance with the Luo

coalescence kernel [49]. As a result, the BSD for $S_{72}$ remains the narrowest, with most bubbles retaining their initial size (5 mm) and only a limited shift toward larger bins. These findings demonstrate that such performance of the $S_{72}$ distributor arises directly from its microjet design, which governs both the initial bubble formation and the subsequent evolution of the bubble population under a turbulence-limited environment.

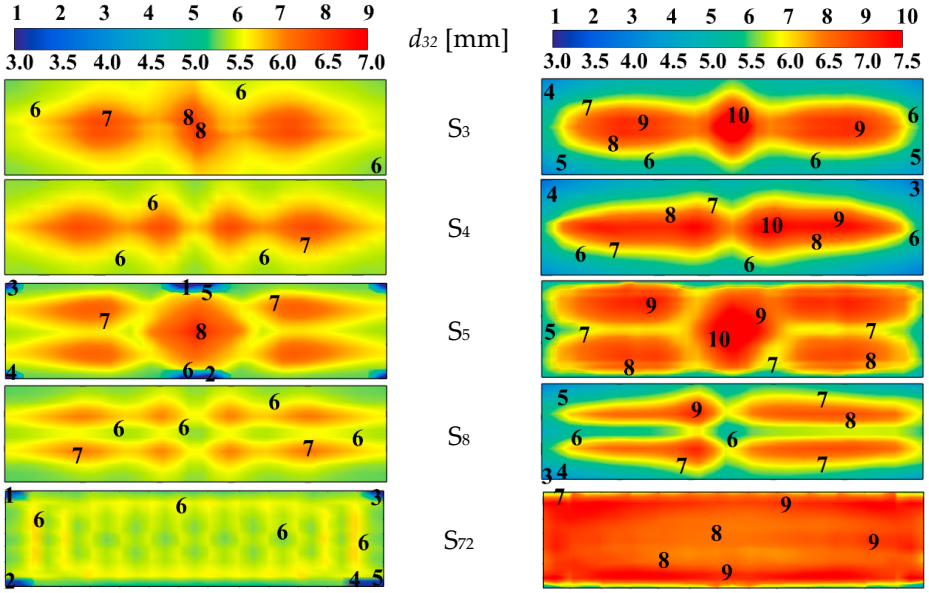


**Figure 8.** Effect of sparger on local BSD at H = 22.5 cm under (**a**) $U_g$ = 0.0014 m/s and (**b**) $U_g$ = 0.0073 m/s. Color contours represent bubble size variation within the measurement plane, highlighting regions of coalescence near the sparger center.

Overall, increasing the number of smaller openings promoted uniform flow regimes and narrowed BSD, particularly at low $U_g$. Despite the same total opening area (2.88 $cm^2$) of all spargers and initial bubble size (5 mm), these findings highlight that the spatial arrangement and size of openings lead a decisive influence on BSD.

Gas holdup is one of the key hydrodynamic parameters of bubble columns because it helps to identify the flow regime in the bubble column and to determine the gas–liquid interfacial area. In this study, Equation (18) is used to calculate overall gas holdup, and its dependence on sparger type is investigated. All the spargers demonstrated different BSD, which is a crucial factor to control the overall gas holdup. As depicted in Figure 11, with increasing numbers of gas openings, overall gas holdup was increased (follows as $S_1 < S_3 < S_4 < S_5 < S_8 < S_{72}$). This could be attributed to increasing concentrations of dense phase (smaller bubbles) and enhanced gas phase dispersion in liquid. Even though the initial bubble size set at each sparger was similar, BSD varied for spargers. Larger bubbles rise quickly; on the other hand, smaller bubbles moving slowly exhibit higher residence time and experience comparatively higher drag force existing between both phases. Also, increasing numbers of plumes may increase the interaction between bubbles, which may offer hindrance to the rising bubbles. This behavior contributes to increasing the overall gas holdup. At low and high $U_g$ values, overall gas holdup resulting from $S_{72}$ was approximately 1.55 times greater than that of $S_1$. $U_g$ is an indispensable factor affecting overall gas holdup strongly; with increase in $U_g$, gas holdup also increased. At higher $U_g$ values, the overall gas holdup appeared nearly independent in the range of $S_4$–$S_8$, which can be credited to insignificant variation in the BSD under these conditions (Figure 9). However, at lower $U_g$, relatively more effect of sparger on the overall gas holdup was found. Moreover, the presently obtained overall gas holdup was further

verified with experimental-based correlation proposed by Kumar et al. [78]. For example, the predicted results of $S_{72}$ were $0.608 \times 10^{-2}$ and $2.967 \times 10^{-2}$ at lower and higher $U_g$ values, respectively, while correlation calculated $0.61 \times 10^{-2}$ and $3.1 \times 10^{-2}$ under similar conditions. This comparison is presented for $S_{72}$ because it has some resemblance with the experimentally used gas sparger.

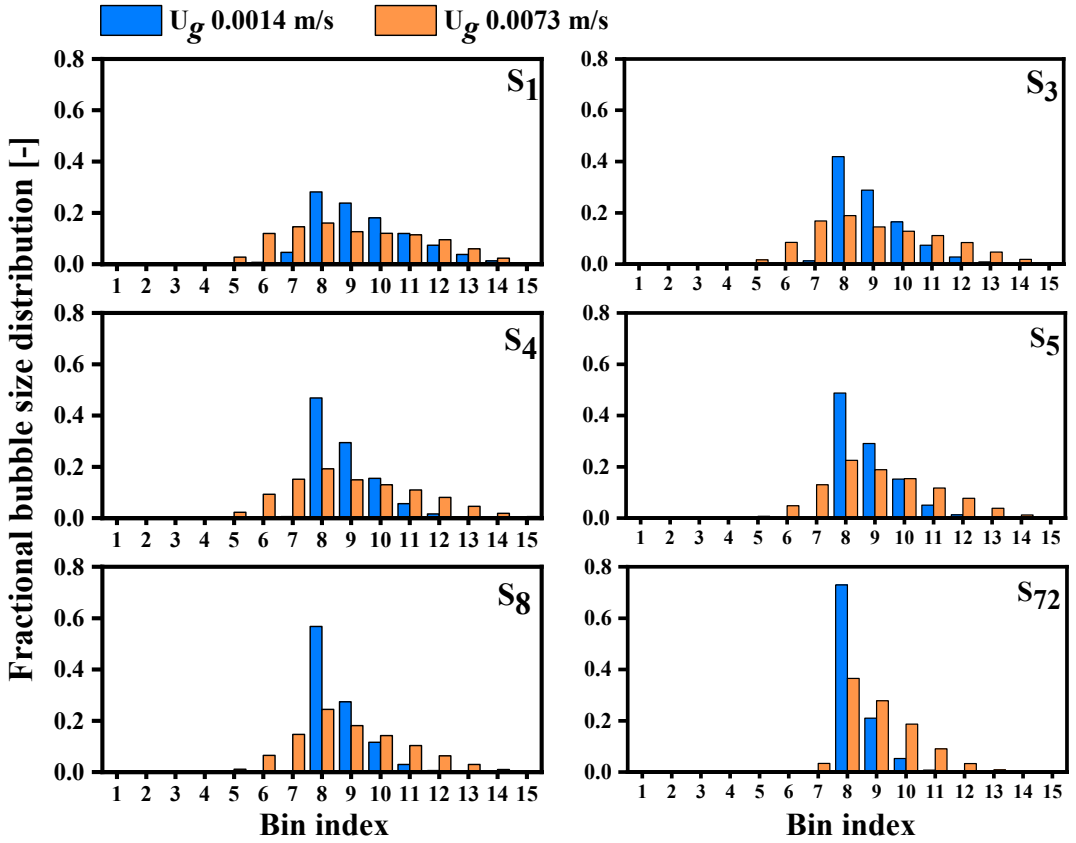


**Figure 9.** Fractional BSD for different spargers at different $U_g$ values.

In a gas–liquid system, higher interfacial area is a desirable condition that gives enhanced rate of mass transfer between phases. Like gas holdup and BSD, interfacial area also strongly depends upon the sparger type and operating conditions. In the present study, the influence of sparger and $U_g$ on gas–liquid interfacial area is investigated and plotted in Figure 12, which was calculated using Equation (37). According to this equation, when the volume fraction of either phase approaches to 1, this results in an interfacial area equal to 0.

$$a = 6\frac{\sum_i \alpha_i(1-\sum_i \alpha_i)}{d_{32}} \tag{37}$$

As depicted in Figure 12, both the $U_g$ and number of gas openings led the positive effect on gas–liquid interfacial area. As discussed earlier, gas holdup and $d_{32}$ increased with increasing gas flow rate. An obvious difference between the interfacial area at low and high $U_g$ values demonstrates that $U_g$ has a significant effect on the gas holdup compared with $d_{32}$. While discussing the effect of the sparger, it seemed that when increasing the number of gas openings, the gas–liquid interfacial area also increased, which can be attributed to fact of smaller bubbles distributed uniformly in the column. Moreover, due to this, the overall gas holdup also increased; therefore, both of these parameters contributed to increasing the interfacial area. This behavior is consistent with the generalization of a higher interfacial area in the bubbly flow regime, where smaller gas bubbles spread more uniformly and create several interfaces with the liquid phase. These results demonstrate

that the effect of $S_{72}$ on interfacial area is relatively low at high $U_g$, which could be explained by the increase in overall bubble size with increasing $U_g$. The present CFD model was also verified by comparing the predicted interfacial area obtained for $S_{72}$ with the experimental-based correlation proposed by Akita et al. [79], which is valid over different square cross-section bubble columns, superficial gas velocities, and different porous-type spargers. For example, the predicted results of $S_{72}$ were 6.27 $m^{-1}$ and 26.3 $m^{-1}$ at lower and higher $U_g$ values, respectively, while correlation calculated 6.58 $m^{-1}$ and 31.76 $m^{-1}$ under the similar conditions. A discrepancy in both values could possibly be attributed to different geometric layouts; however, the correlation can also be applied to rectangular columns within a certain range.

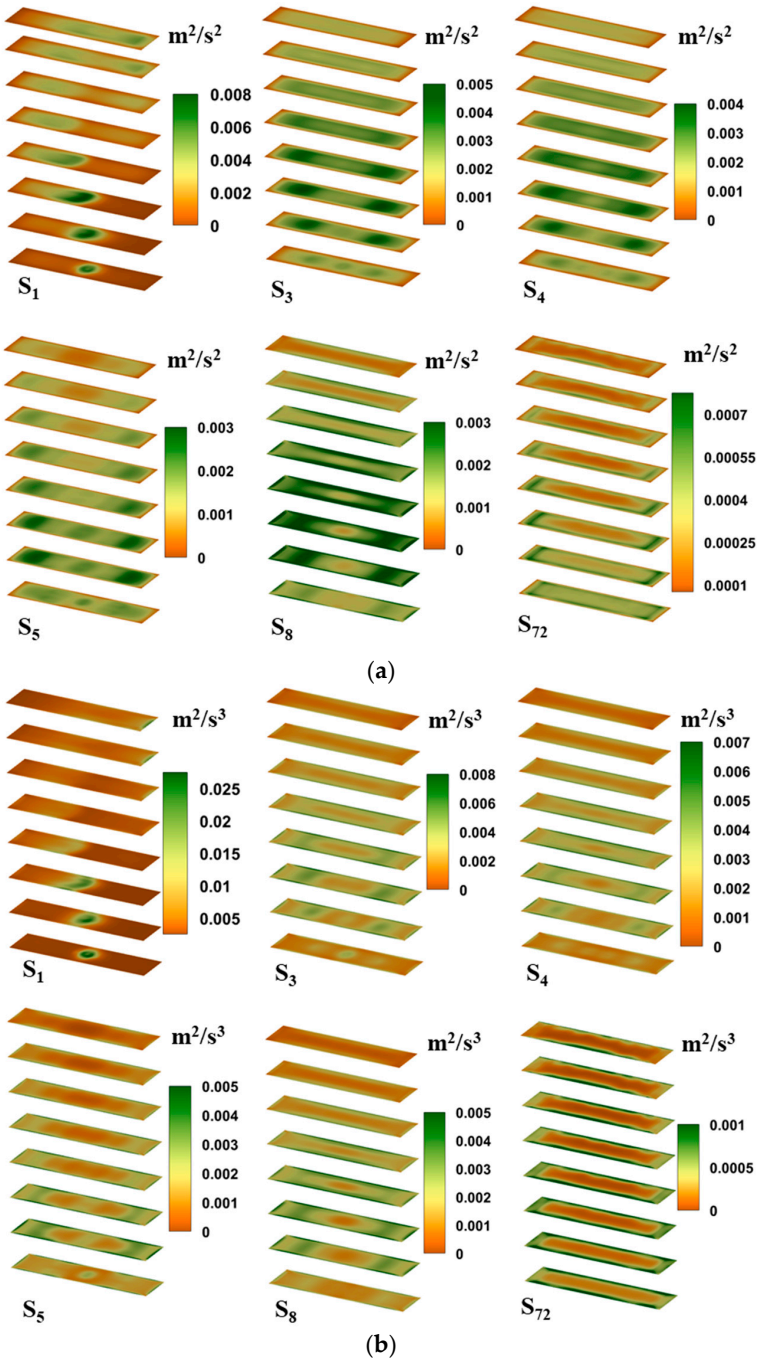


**Figure 10.** Distribution of (**a**) turbulent kinetic energy ($k$) and (**b**) turbulence dissipation rate ($\varepsilon$) under $U_g$ = 0.0014 m/s at axial positions of 5 cm, 10 cm, 15 cm, 20 cm, 25 cm, 30 cm, 35 cm, and 40 cm.

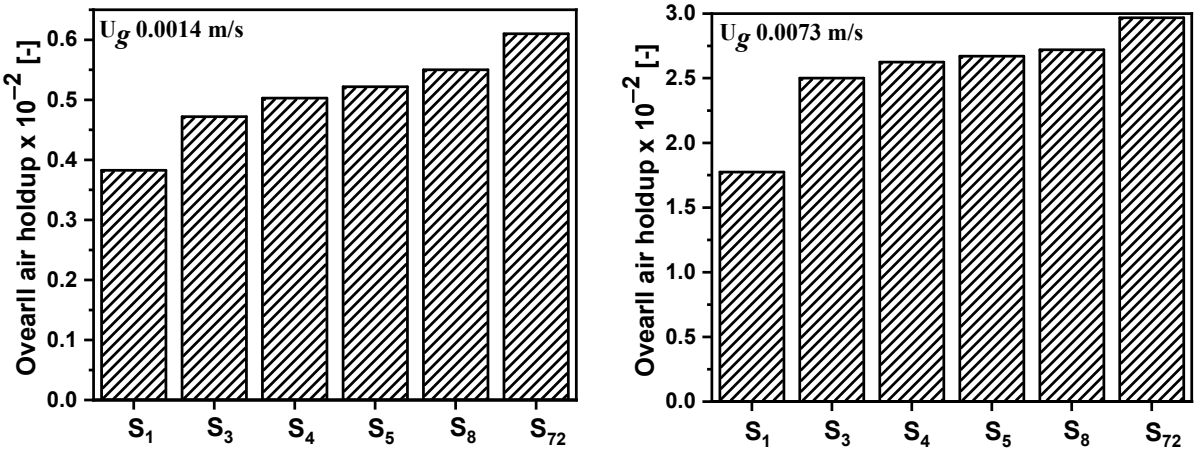


**Figure 11.** Effect of sparger on overall air holdup at different $U_g$ values.

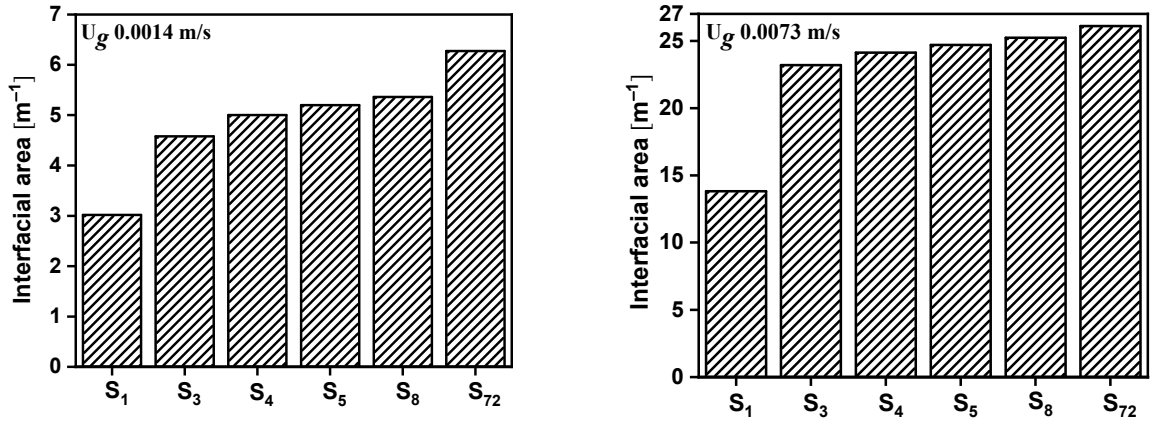


**Figure 12.** Effects of sparger on gas–liquid interfacial area at different $U_g$ values.

#### 4.2.2. Effect of Horizontal Baffles

The actual bubble column was sectionalized by inserting horizontal baffle-based hydrodynamic considerations in two different configurations, known as Config-A and Config-B. In Config-A, three alternate baffles occupying 2% of the total volume were periodically and equally spaced, leading to a zig-zag flow and interrupting the development of a continuous vertical gas plume. This equal spacing ensured a uniform interaction of each baffle with the growing plume, preventing early plume stabilization and promoting enhanced mixing throughout the column. In Config-B, equally spaced baffles occupying 1.7% of the total volume were arranged in such a manner that the central space for flow was narrowed in the lower and upper regions of column, and a baffle was inserted in the middle of the column as an obstruction to redistribute the rising bubbles. This configuration was intended to control plume expansion, promote bubble redistribution and bubble–liquid interaction, and regulate bubble residence behavior across the column height.

Instead of sparging the gas in the center only, spargers $S_4$ and $S_8$ were selected for Config-A and Config-B, respectively, to achieve an improved dispersion of gas over a cross-section of the column. The details of the configurations are illustrated in Figure 13a,b. Similar operating and boundary conditions were adopted for their simulation, and a no-slip condition was set on the surface of the baffles.

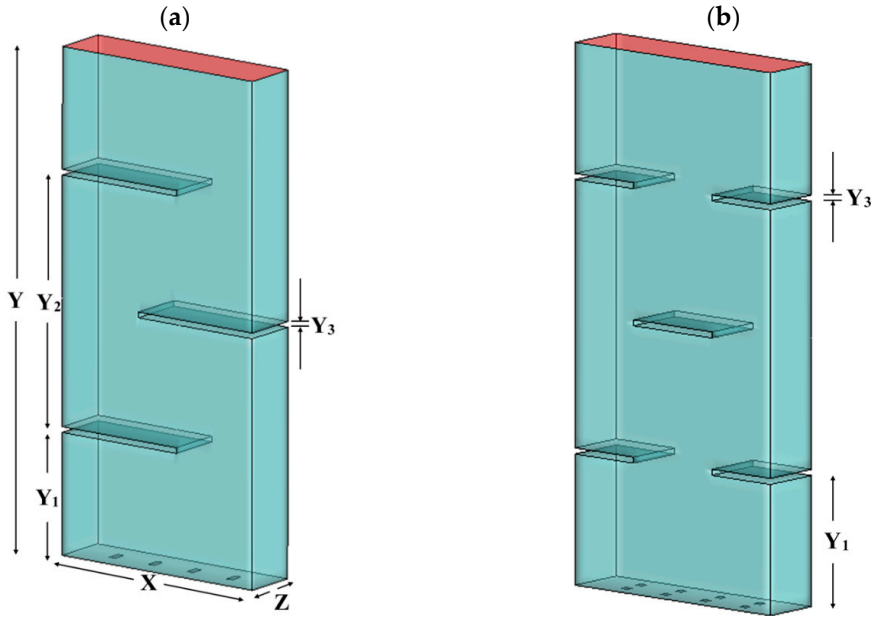


**Figure 13.** 3D schematic representation of bubble column: (**a**) Config-A and (**b**) Config-B.

The CFD results of the time-averaged liquid flow pattern in the baffled columns were compared with those in corresponding actual columns denoted as WHB-($S_4$) and WHB-($S_8$) (consisting of spargers $S_4$ and $S_8$, respectively) in Figure 14. In both columns, rising gas bubbles entrained the surrounding liquid, forming downward-moving vortexes near the walls upon detachment. These vortexes promote the mixing of fluid, which is very important in heat and mass transfer applications. It was observed that, at higher $U_g$, comparatively small vortexes were formed, which could be attributed to quicker detachment of gas bubbles from entrained liquid. Notably, a similar pattern of vortexes either at low or high velocity was observed in both WHB-($S_4$) and WHB-($S_8$), indicating the negligible role of sparger configuration on liquid flow pattern. In contrast, bubble columns equipped with horizontal baffles resulted in improved liquid mixing and ultimately higher gas–liquid interactions. Horizontal baffles enhanced mixing and gas–liquid interactions by breaking large vortexes into smaller ones within inter-baffle regions. As shown in Figure 14a,b, separate units between the two consecutive baffles act as continuous stirred tank reactor (CSTR), as already debated by Doshi et al. [12]. The phenomenon of suppressing global mixing, as observed in columns WHB-($S_4$) and WHB-($S_8$), is favorable for all the separation processes carried out at industrial scale, and a higher efficiency of the process can be expected. It may be noted that a distinct flow behavior was obtained for Config-A, which developed a single vortex between the baffles. In Config-B, a pair of smaller vortexes was produced, which further enhanced the degree of fluid mixing. Such induced vortexes extend the contact time between both phases, and they also help the gas phase to disperse more effectively in the liquid phase.

In Figure 15a, the turbulent kinetic energy ($k$) contours show that at $U_g$ = 0.0014 m/s, both Config-A and Config-B exhibit localized turbulence near the sparger, and the addition of horizontal baffles generated distinct high-energy regions just below each baffle due to flow impingement. Figure 15b depicts that at $U_g$ = 0.0073 m/s, the overall turbulence intensity was increased, with more uniform energy distribution. This indicates that horizontal baffles effectively break large eddies into smaller structures, enhance local mixing, and stabilize the flow field.

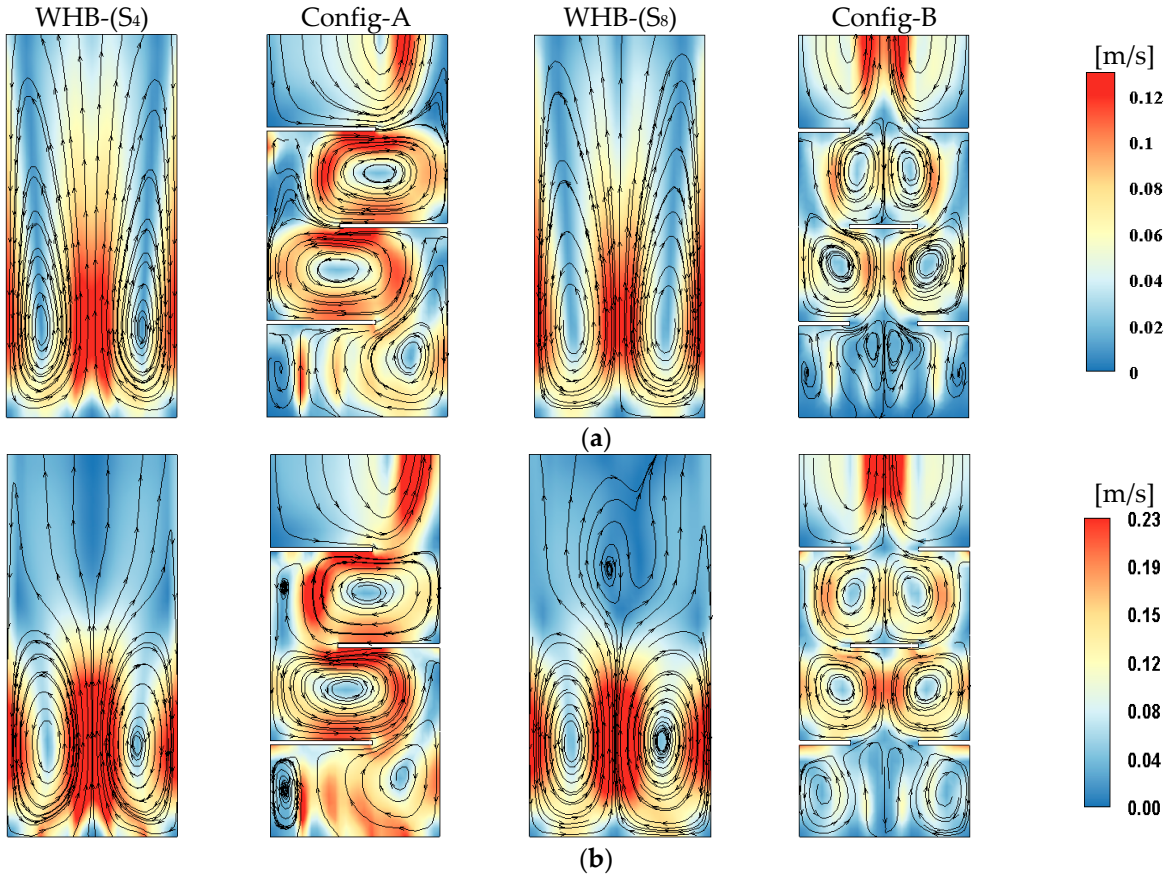


**Figure 14.** Water velocity field at vertical sectional plane under (**a**) $U_g$ = 0.0014 m/s and (**b**) $U_g$ = 0.0073 m/s.

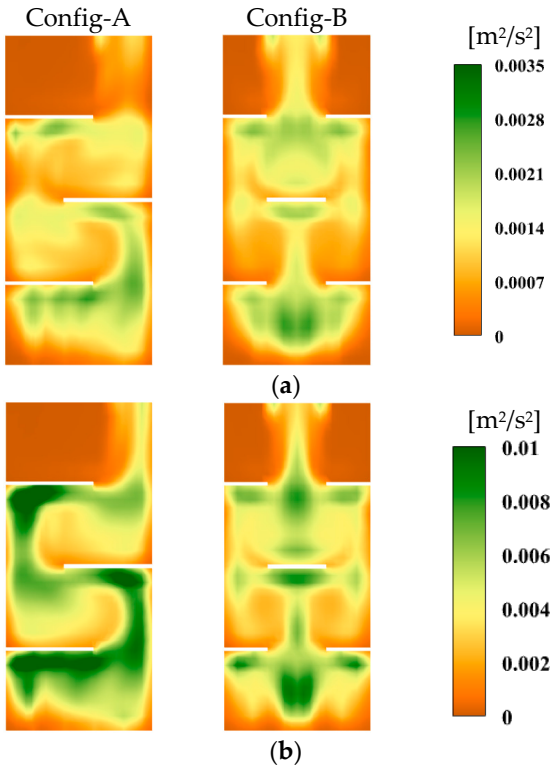


**Figure 15.** Turbulent kinetic energy distribution at vertical sectional plane (**a**) under $U_g$ = 0.0014 m/s and (**b**) under $U_g$ = 0.0073 m/s.

Figure 16 shows the local bubble size distribution for both configurations. Both the configurations exhibit relatively stronger coalescence directly beneath each horizontal baffle, which continues with column height. This behavior is consistent with the results of turbulent kinetic energy (Figure 15), where distinct high-energy regions were observed below the baffles due to flow impingement. These high-turbulence zones increase bubble–bubble collision frequency and shorten film drainage time, promoting coalescence and resulting in larger local bubble diameters according to the Luo coalescence kernel [49]. Additionally, an increase in gas velocity further enhanced bubble size throughout the column by intensifying turbulence and collision rates.

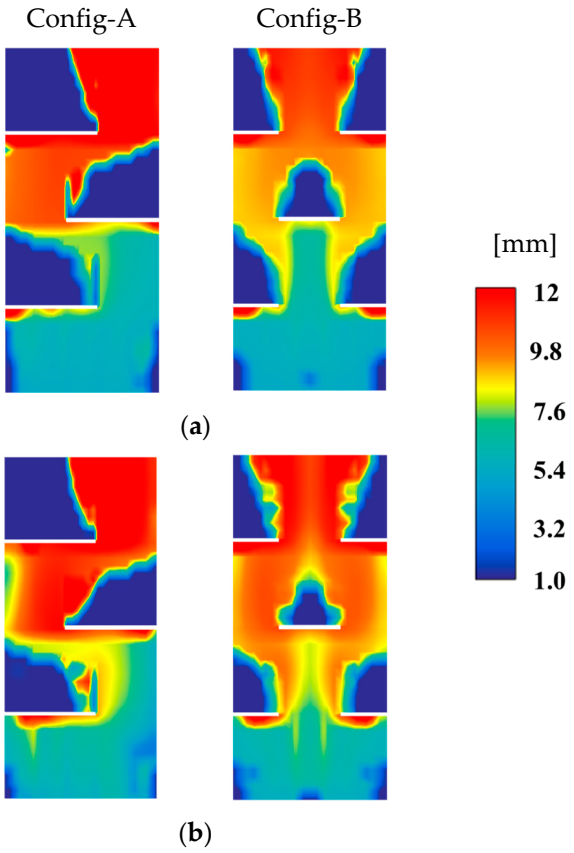


**Figure 16.** Local BSD at vertical sectional plane under (**a**) $U_g$ = 0.0014 m/s and (**b**) $U_g$ = 0.0073 m/s.

Fractional BSD in baffled columns, i.e., Config-A and Config-B, is depicted in Figure 17. At low $U_g$, the fraction of smaller bins was minimal, indicating dominance of coalescence. However, at high $U_g$, slightly increased bubble breakage was found in the form of a minute shift towards small bubbles. Overall, $U_g$ had an insignificant effect on the fractional distribution of large bubbles. The baffles promoted coalescence and resulted in a wide range of large bubble sizes, likely due to bubble accumulation beneath the horizontal baffles, which increased collision frequency and ultimately enhanced coalescence.

According to Equation (37), both the gas holdup and $d_{32}$ strongly affect the interfacial area. Insertion of horizontal baffles in open columns significantly increased the overall gas holdup, which was 2.5 and 1.63 times higher in Config-A and 1.87 and 1.5 times higher in Config-B at low and high $U_g$ values, respectively. The increase in overall gas holdup could be attributed to two factors, which are reduction in the overall flow volume due to space occupied by the baffles and the obstruction of bubble rise caused by the baffles, enhancing bubble residence time. As previously mentioned, enhanced bubble coalescence was observed in the baffled columns, leading to the formation of larger bubbles, which could potentially reduce the available gas–liquid interfacial area. As shown in Figure 18a,

Config-A increased the interfacial area under both $U_g$ conditions, indicating that gas holdup dominated over $d_{32}$. The effect was more pronounced at low $U_g$ due to the larger change in holdup. In Config-B, the interfacial area increased relative to the WHB-($S_8$) at low $U_g$ but decreased at high $U_g$, demonstrating that gas holdup governs $d_{32}$ at low $U_g$, whereas this influence weakens at higher velocity (Figure 18b).

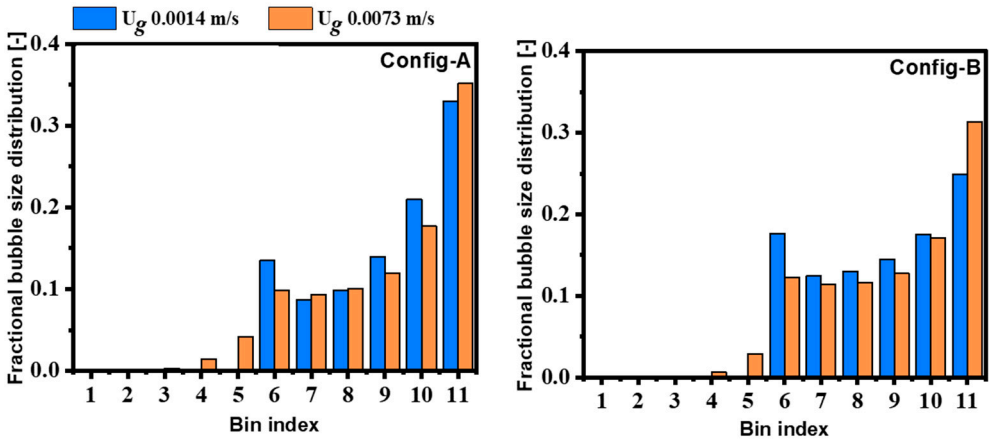


**Figure 17.** Effect of horizontal baffles on fractional BSD.

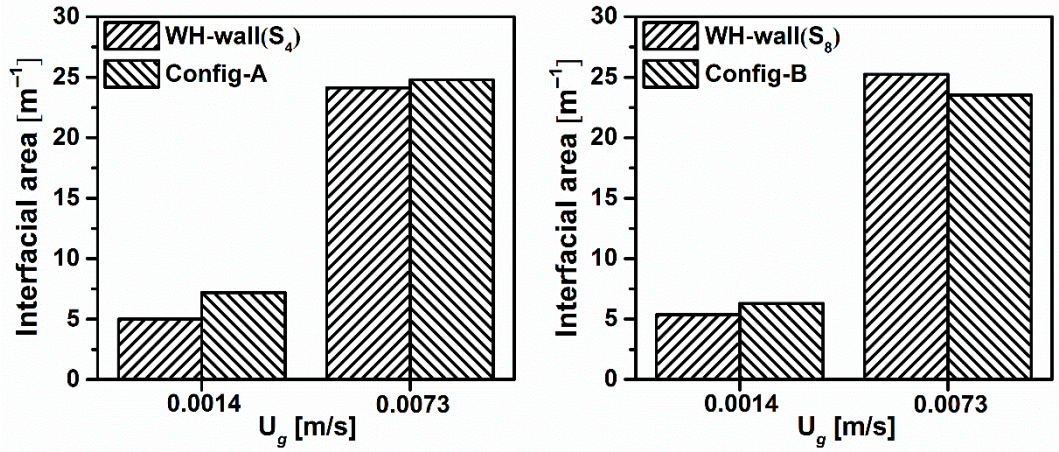


**Figure 18.** Effect of horizontal baffles on gas–liquid interfacial area under (**a**) $U_g$ = 0.0014 m/s and (**b**) $U_g$ = 0.0073 m/s.

## 5. Conclusions

The coupled CFD-PBM framework was used to study the hydrodynamic characteristics in an air–water flat bubble column, which were validated experimentally. Subsequently, the validated CFD model was extended to investigate the effect of different gas sparger types and the inclusion of horizontal baffles on the overall bubble size distribution, gas phase distribution, overall gas holdup, and interfacial area. Despite the same initial bubble size (5 mm) used for all spargers, differences in numbers, sizes and arrangements of gas openings led to variation in the initial spatial distribution of bubbles and the turbulence near the inlet. These variations governed the early and overall breakage and coalescence phenomena, ultimately shaping the overall bubble size distribution. It was found that overall gas holdup and interfacial area were increased with increasing numbers and decreases in the size of individual gas opening in the sparger. The gas holdup and interfacial area obtained by $S_{72}$ were 1.55 and 2 times that of $S_1$. Both the sparger and $U_g$ showed significant effects on BSD as well; however, in the range of $S_4$–$S_8$, the sparger's effect was

not noticeable. Spargers with fewer and larger openings produced high-momentum plumes and elevated turbulence, promoting early breakage and coalescence and widening the BSD. Contrastingly, micro-opening sparger $S_{72}$ generated low-turbulence plumes that minimized shear-induced breakup and turbulence-driven coalescence, yielding the narrowest BSD. Overall, the sparger design dominates the early evolution of BSD through its control of bubble distribution and inlet turbulence.

The baffles in bubble columns (Config-A and Config-B) resulted in improved liquid mixing and strengthened gas–liquid interactions. The flow impingement beneath each baffle intensified local turbulent kinetic energy, which increased bubble–bubble collision frequency and promoted coalescence, ultimately producing larger bubbles. Although the baffles increased gas holdup, the interfacial area did not vary significantly, which is credited to enhanced coalescence.

These findings have direct practical relevance for the design and scale-up of bubble columns. Micro-opening spargers such as $S_{72}$ achieve enhanced gas holdup and interfacial area, thereby improving mass transfer. Inclusion of horizontal baffles (Config-A or Config-B) is beneficial for increasing gas holdup, promoting coalescence, and enhancing turbulence, which can be a good choice in absorption columns. Further, application of micro-opening spargers and baffles can be integrated to maintain the small bubble size as well as enhanced turbulence and phase mixing.

The insights obtained from the present model demonstrate its applicability to investigate the necessary hydrodynamic characteristics essential for designing and scaling-up multiphase contacting devices. However, this study is limited to Newtonian and low-viscosity liquids and therefore does not account for the rheological effects present in non-Newtonian or highly viscous systems. These aspects could be potential considerations for future studies.

**Author Contributions:** Conceptualization, M.A. and L.Y.; Methodology, M.A.; Software, M.A., I.N.U., J.K., S.A., and L.Y.; Validation, M.A.; Formal analysis, I.N.U. and A.Q.L.; Investigation, A.S.J.; Data curation, J.K. and S.A.; Writing—original draft, M.A.; Writing—review and editing, A.Q., A.Q.L., L.Y., and A.S.J.; Visualization, A.Q. and S.A.; Supervision, L.Y. All authors have read and agreed to the published version of the manuscript.

**Funding:** This research was funded by the National Natural Science Foundation of China (21878010).

**Data Availability Statement:** The original contributions presented in this study are included in the article. Further inquiries can be directed to the corresponding author.

**Acknowledgments:** The authors acknowledge the College of Chemical Engineering, Beijing University of Chemical Technology, Beijing 100029, China, for providing access to research resources.

**Conflicts of Interest:** The authors declare no conflict of interest.

## Nomenclature

| | | | |
|---|---|---|---|
| $a$ | Interfacial area [1/m] | $\lambda$ | Bulk viscosity [Kg/ms] |
| $B$ | Birth term | $\mu$ | Viscosity [Kg/m s] |
| $C_D$ | Drag coefficient | $\xi$ | Dimensionless eddy size |
| $C_L$ | Lift coefficient | $\rho$ | Phase density [Kg/m$^3$] |
| $C_{VM}$ | Virtual mass coefficient | $\sigma$ | Surface tension [N/m] |
| $C_W$ | Wall lubrication coefficient | $\omega_c\ (v,\ v')$ | Collision frequency |
| $C_\mu$ | Constant in $k$-$\varepsilon$ turbulence model | | |
| $D$ | Death term | Subscripts | |
| $d$ | Bubble diameter [m] | | |
| $d_d$ | Diameter of daughter bubble [m] | b | Bubble |

| | |
|---|---|
| $d_{par}$ | Diameter of parent bubble [m] |
| $d_{32}$ | Sauter mean diameter [m] |
| $f_i$ | Individual bin size fraction of $i^{th}$ bin |
| $f_{bv}$ | Volume fraction of parent bubble in one daughter bubble |
| $\boldsymbol{F_q}$ | Total interphase force [N/m$^3$] |
| $\boldsymbol{F_D}$ | Drag force [N/m$^3$] |
| $\boldsymbol{F_L}$ | Lift force [N/m$^3$] |
| $\boldsymbol{F_{VM}}$ | Virtual mass force [N/m$^3$] |
| $\boldsymbol{F_W}$ | Wall lubrication force [N/m$^3$] |
| $\vec{g}$ | Gravity [m/s$^2$] |
| $\overline{\overline{I}}$ | Identity matrix |
| $k$ | Turbulent kinetic energy [m$^2$/s$^2$] |
| $m$ | Mean number of daughter bubbles produced from breakage |
| $n$ | Bubble number density [1/m$^3$] |
| $P_c(v, v')$ | Coalescence efficiency |
| $r_{br}$ | Breakup rate [1/m$^3$ s] |
| $r_c$ | Coalescence rate [m$^3$/s] |
| $S_i$ | Source term accounting birth and death terms of bubbles [kg/m$^3$ s] |
| $U_g$ | Superficial gas velocity [m/s] |
| $U_t$ | Terminal velocity [m/s] |
| $\overline{\boldsymbol{u}}$ | Characteristic velocity bubble collision [m/s] |
| $\boldsymbol{v}$ | Velocity vector [m/s] |

Greek Letters

| | |
|---|---|
| $\alpha$ | Void fraction [-] |
| $\gamma$ | Length scale of hitting eddy [m] |
| $\varepsilon$ | Turbulence dissipation rate [m$^2$/s$^3$] |

| | |
|---|---|
| $i$ | $i^{th}$ bin |
| $p$ | $p^{th}$ phase |
| $q$ | $q^{th}$ phase |

Superscripts

| | |
|---|---|
| $br$ | Breakage |
| $c$ | Coalescence |
| $crit$ | Critical |
| $eff$ | Effective |
| $l$ | Laminar |
| $t$ | Turbulent |

Dimensionless numbers

| | |
|---|---|
| $Eo$ | Eötvös number, $Eo = \frac{g(\rho_p - \rho_q)d_b^2}{\sigma}$ |
| $Mo$ | Morton number, $Mo = \frac{\mu_p^4 g(\rho_p - \rho_q)}{\rho_p^2 \sigma^3}$ |
| $Re$ | Reynold number, $Re = \frac{\rho_p(\boldsymbol{v}_p - \boldsymbol{v}_q)d_b}{\mu_p}$ |
| $We$ | Weber number, $We = \frac{\rho_p d_i(\overline{\boldsymbol{u}})^2}{\sigma}$ |

Abbreviations

| | |
|---|---|
| BSD | Bubble size distribution |
| PBM | Population balance modeling |
| SIMPLE | Semi-Implicit Method for Pressure-Linked Equations |

## References


1. Chew, K.W.; Chia, S.R.; Show, P.L.; Yap, Y.J.; Ling, T.C.; Chang, J.-S. Effects of water culture medium, cultivation systems and growth modes for microalgae cultivation: A review. *J. Taiwan Inst. Chem. Eng.* **2018**, *91*, 332–344. [CrossRef]
2. Contreras-Gómez, A.; López-Rosales, L.; Martínez-Burgos, J.; Molina-Miras, A.; Cerón-García, M.C.; Sánchez-Mirón, A.; García-Camacho, F. Valorisation of seawater desalination brine via cultivation of a halotolerant microalga in bubble column photobioreactors. *Bioresour. Technol.* **2026**, *439*, 133261. [CrossRef] [PubMed]
3. Vitankar, V.S.; Joshi, J.B. A Comprehensive One-Dimensional Model for Prediction of Flow Pattern in Bubble Columns. *Chem. Eng. Res. Des.* **2002**, *80*, 499–512. [CrossRef]
4. Vijayan, M.; Schlaberg, H.; Wang, M. Effects of sparger geometry on the mechanism of flow pattern transition in a bubble column. *Chem. Eng. J.* **2007**, *130*, 171–178. [CrossRef]
5. Díaz, M.E.; Montes, F.J.; Galán, M.A. Influence of Aspect Ratio and Superficial Gas Velocity on the Evolution of Unsteady Flow Structures and Flow Transitions in a Rectangular Two-Dimensional Bubble Column. *Ind. Eng. Chem. Res.* **2006**, *45*, 7301–7312. [CrossRef]
6. Li, W.; Zhong, W.; Jin, B.; Lu, Y.; He, T. Flow patterns and transitions in a rectangular three-phase bubble column. *Powder Technol.* **2014**, *260*, 27–35. [CrossRef]
7. Chen, P.; Sanyal, J.; Duduković, M.P. Numerical simulation of bubble columns flows: Effect of different breakup and coalescence closures. *Chem. Eng. Sci.* **2005**, *60*, 1085–1101. [CrossRef]
8. Kulkarni, A.A.; Ekambara, K.; Joshi, J.B. On the development of flow pattern in a bubble column reactor: Experiments and CFD. *Chem. Eng. Sci.* **2007**, *62*, 1049–1072. [CrossRef]
9. Kantarci, N.; Borak, F.; Ulgen, K.O. Bubble column reactors. *Process Biochem.* **2005**, *40*, 2263–2283. [CrossRef]

10. Pourtousi, M.; Ganesan, P.; Sandaran, S.C.; Sahu, J.N. Effect of ring sparger diameters on hydrodynamics in bubble column: A numerical investigation. *J. Taiwan Inst. Chem. Eng.* **2016**, *69*, 14–24. [CrossRef]
11. Li, Y.; Zhang, X.; Liu, S.; Li, C.; Cui, Y.; Shi, X.; Su, X.; Gao, J.; Lan, X. Numerical simulation of flow characteristics in microbubble column reactors with two different tubular gas spargers. *Chem. Eng. Process. Process Intensif.* **2025**, *216*, 110431. [CrossRef]
12. Doshi, Y.K.; Pandit, A.B. Effect of internals and sparger design on mixing behavior in sectionalized bubble column. *Chem. Eng. J.* **2005**, *112*, 117–129. [CrossRef]
13. Bhole, M.R.; Roy, S.; Joshi, J.B. Laser Doppler Anemometer Measurements in Bubble Column: Effect of Sparger. *Ind. Eng. Chem. Res.* **2006**, *45*, 9201–9207. [CrossRef]
14. Gemello, L.; Plais, C.; Augier, F.; Cloupet, A.; Marchisio, D.L. Hydrodynamics and bubble size in bubble columns: Effects of contaminants and spargers. *Chem. Eng. Sci.* **2018**, *184*, 93–102. [CrossRef]
15. McClure, D.D.; Wang, C.; Kavanagh, J.M.; Fletcher, D.F.; Barton, G.W. Experimental investigation into the impact of sparger design on bubble columns at high superficial velocities. *Chem. Eng. Res. Des.* **2016**, *106*, 205–213. [CrossRef]
16. Marchini, S.; Bieberle, A.; Caggia, V.; Schubert, M.; Brunazzi, E.; Hampel, U. Axially resolved measurement of axial gas dispersion in bubble columns via gas flow modulation technique. *Chem. Eng. J.* **2025**, *517*, 163481. [CrossRef]
17. Kalaga, D.V.; Pant, H.J.; Dalvi, S.V.; Joshi, J.B.; Roy, S. Investigation of Hydrodynamics in Bubble Column with Internals Using Radioactive Particle Tracking (RPT). *Aiche J.* **2017**, *63*, 4881–4894. [CrossRef]
18. Xia, Y.K.; Peng, F.F.; Wolfe, E. CFD simulation of alleviation of fluid back mixing by baffles in bubble column. *Miner. Eng.* **2006**, *19*, 925–937. [CrossRef]
19. Alvaré, J.; Al-Dahhan, M.H. Gas Holdup in Trayed Bubble Column Reactors. *Ind. Eng. Chem. Res.* **2006**, *45*, 3320–3326. [CrossRef]
20. Liu, S.; Liang, J.; Li, Q.; Yu, H.; Wang, H.; Li, X.; Yang, C. Effects of internals on macroscopic fluid dynamics in a bubble column. *Chin. J. Chem. Eng.* **2025**, *77*, 19–29. [CrossRef]
21. Bhusare, V.H.; Dhiman, M.K.; Kalaga, D.V.; Roy, S.; Joshi, J.B. CFD simulations of a bubble column with and without internals by using OpenFOAM. *Chem. Eng. J.* **2017**, *317*, 157–174. [CrossRef]
22. Qudoos, A.; Chew, T.L.; Abro, M.; Oh, P.C.; Anbealagan, L.D.; Bustam, M.A.; Ho, C.D.; Jawad, Z.A.; Ng, Q.H. Review on Computational Fluid Dynamics (CFD) Modeling and Simulation of $CO_2$ Adsorption. *Results Eng.* **2025**, *28*, 107336. [CrossRef]
23. Fletcher, D.F.; McClure, D.D.; Kavanagh, J.M.; Barton, G.W. CFD simulation of industrial bubble columns: Numerical challenges and model validation successes. *Appl. Math. Model.* **2017**, *44*, 25–42. [CrossRef]
24. Ma, T.; Ziegenhein, T.; Lucas, D.; Fröhlich, J. Large eddy simulations of the gas–liquid flow in a rectangular bubble column. *Nucl. Eng. Des.* **2016**, *299*, 146–153. [CrossRef]
25. Islam, M.T.; Nguyen, A.V.; Afzal, A. Bubble's rise characteristics in shear-thinning xanthan gum solution: A numerical analysis. *J. Taiwan Inst. Chem. Eng.* **2022**, *132*, 104219. [CrossRef]
26. Liang, X.-F.; Pan, H.; Su, Y.-H.; Luo, Z.-H. CFD-PBM approach with modified drag model for the gas–liquid flow in a bubble column. *Chem. Eng. Res. Des.* **2016**, *112*, 88–102. [CrossRef]
27. Guo, X.; Chen, C. Simulating the impacts of internals on gas–liquid hydrodynamics of bubble column. *Chem. Eng. Sci.* **2017**, *174*, 311–325. [CrossRef]
28. Buwa, V.V.; Ranade, V.V. Mixing in Bubble Column Reactors: Role of Unsteady Flow Structures. *Can. J. Chem. Eng.* **2008**, *81*, 402–411. [CrossRef]
29. Li, Q.; Cheng, J.; Yang, C.; Mao, Z.-S. Simulation of a Bubble Column by Computational Fluid Dynamics and Population Balance Equation Using the Cell Average Method. *Chem. Eng. Technol.* **2017**, *40*, 1792–1801. [CrossRef]
30. Shen, X.; Jia, Z.; Zhang, H.; Wang, T. Numerical simulation of volumetric mass transfer coefficients in slurry bubble columns with a CFD-PBM coupled model. *Chem. Eng. Sci.* **2025**, *318*, 122153. [CrossRef]
31. Liu, Y.; Hinrichsen, O. Study on CFD–PBM turbulence closures based on k–ε and Reynolds stress models for heterogeneous bubble column flows. *Comput. Fluids* **2014**, *105*, 91–100. [CrossRef]
32. Syed, A.H.; Boulet, M.; Melchiori, T.; Lavoie, J.M. CFD Simulations of an Air-Water Bubble Column: Effect of Luo Coalescence Parameter and Breakup Kernels. *Front. Chem.* **2017**, *5*, 68. [CrossRef] [PubMed]
33. Sattar, M.A.; Naser, J.; Brooks, G. Numerical simulation of two-phase flow with bubble break-up and coalescence coupled with population balance modeling. *Chem. Eng. Process.* **2013**, *70*, 66–76. [CrossRef]
34. Bannari, R.; Kerdouss, F.; Selma, B.; Bannari, A.; Proulx, P. Three-dimensional mathematical modeling of dispersed two-phase flow using class method of population balance in bubble columns. *Comput. Chem. Eng.* **2008**, *32*, 3224–3237. [CrossRef]
35. Díaz, M.E.; Iranzo, A.; Cuadra, D.; Barbero, R.; Montes, F.J.; Galán, M.A. Numerical simulation of the gas–liquid flow in a laboratory scale bubble column. *Chem. Eng. J.* **2008**, *139*, 363–379. [CrossRef]
36. Selma, B.; Bannari, R.; Proulx, P. A full integration of a dispersion and interface closures in the standard k-e model of turbulence. *Chem. Eng. Sci.* **2010**, *65*, 5417–5428. [CrossRef]
37. Juliá, J.E.; Hernández, L.; Chiva, S.; Vela, A. Hydrodynamic characterization of a needle sparger rectangular bubble column: Homogeneous flow, static bubble plume and oscillating bubble plume. *Chem. Eng. Sci.* **2007**, *62*, 6361–6377. [CrossRef]

38. Pfleger, D.; Gomes, S.; Gilbert, N.; Wagner, H.G. Hydrodynamic simulations of laboratory scale bubble columns fundamental studies of the Eulerian–Eulerian modelling approach. *Chem. Eng. Sci.* **1999**, *54*, 5091–5099. [CrossRef]
39. Upadhyay, R.K.; Pant, H.J.; Roy, S. Liquid flow patterns in rectangular air-water bubble column investigated with Radioactive Particle Tracking. *Chem. Eng. Sci.* **2013**, *96*, 152–164. [CrossRef]
40. Liu, Y.; Luo, H.; Li, G.; Liu, J. An experimental investigation on bubble-liquid turbulent hydrodynamics in an external-loop airlift bioreactor. *J. Taiwan Inst. Chem. Eng.* **2025**, *175*, 106290. [CrossRef]
41. Gupta, A.; Roy, S. Euler–Euler simulation of bubbly flow in a rectangular bubble column: Experimental validation with Radioactive Particle Tracking. *Chem. Eng. J.* **2013**, *225*, 818–836. [CrossRef]
42. Buwa, V.V.; Deo, D.S.; Ranade, V.V. Eulerian–Lagrangian simulations of unsteady gas–liquid flows in bubble columns. *Int. J. Multiph. Flow* **2006**, *32*, 864–885. [CrossRef]
43. Farzpourmachiani, A.; Shams, M.; Shadaram, A.; Azidehak, F. Eulerian–Lagrangian 3-D simulations of unsteady two-phase gas–liquid flow in a rectangular column by considering bubble interactions. *Int. J. Non-Linear Mech.* **2011**, *46*, 1049–1056. [CrossRef]
44. Anderson, J.D. Governing Equations of Fluid Dynamics. In *Computational Fluid Dynamics: An Introduction*; Wendt, J.F., Ed.; Springer: Berlin/Heidelberg, Germany, 1992; pp. 15–51.
45. Cheng, J.; Yang, C.; Mao, Z.-S. CFD-PBE simulation of premixed continuous precipitation incorporating nucleation, growth and aggregation in a stirred tank with multi-class method. *Chem. Eng. Sci.* **2012**, *68*, 469–480. [CrossRef]
46. Kumar, S.; Ramkrishna, D. On the solution of population balance equations by discretization Part I. A fixed pivot technique. *Chem. Eng. Sci.* **1996**, *51*, 1311–1332. [CrossRef]
47. Besagni, G.; Inzoli, F. Prediction of Bubble Size Distributions in Large-Scale Bubble Columns Using a Population Balance Model. *Computation* **2019**, *7*, 17. [CrossRef]
48. Ramkrishna, D. *Population Balances: Theory and Applications to Particulate Systems in Engineering*; Elsevier: Amsterdam, The Netherlands, 2000.
49. Luo, H. *Coalescence, Breakup and Liquid Circulation in Bubble Column Reactors*; Norwegian Institute of Technology: Trondheim, Norway, 1993.
50. Lehr, F.; Millies, M.; Mewes, D. Bubble-Size distributions and flow fields in bubble columns. *Aiche J.* **2002**, *48*, 2426–2443. [CrossRef]
51. ANSYS, I. *Ansys Fluent Theory Guide*; ANSYS, Inc: Canonsburg, PA, USA, 2021.
52. Wilcox, D.C. *Turbulence Modeling for CFD*; DCW Industries: La Canada, CA, USA, 1998.
53. Launder, B.E.; Spalding, D.B. Paper 8—The Numerical Computation of Turbulent Flows. In *Numerical Prediction of Flow, Heat Transfer, Turbulence and Combustion*; Patankar, S.V., Pollard, A., Singhal, A.K., Vanka, S.P., Eds.; Pergamon: Oxford, UK, 1983; pp. 96–116.
54. Sato, Y.; Sekoguchi, K. Liquid velocity distribution in two-phase bubble flow. *Int. J. Multiph. Flow* **1975**, *2*, 79–95. [CrossRef]
55. Saleh, S.N.; Mohammed, A.A.; Al-Jubory, F.K.; Barghi, S. CFD assesment of uniform bubbly flow in a bubble column. *J. Pet. Sci. Eng.* **2018**, *161*, 96–107. [CrossRef]
56. Wang, L.; Pan, Q.; Chen, J.; Yang, S. CFD-PBM Approach with Different Inlet Locations for the Gas-Liquid Flow in a Laboratory-Scale Bubble Column with Activated Sludge/Water. *Computation* **2017**, *5*, 38. [CrossRef]
57. Li, W.; Zhong, W. CFD simulation of hydrodynamics of gas–liquid–solid three-phase bubble column. *Powder Technol.* **2015**, *286*, 766–788. [CrossRef]
58. Oey, R.S.; Mudde, R.F.; van den Akker, H.E.A. Sensitivity study on interfacial closure laws in two-fluid bubbly flow simulations. *Aiche J.* **2003**, *49*, 1621–1636. [CrossRef]
59. Silva, M.K.; d'Ávila, M.A.; Mori, M. Study of the interfacial forces and turbulence models in a bubble column. *Comput. Chem. Eng.* **2012**, *44*, 34–44. [CrossRef]
60. Grace, J.R. Shapes and Velocities of Single Drops and Bubbles Moving Freely through Immiscible Liquids. *Chem. Eng. Res. Des.* **1976**, *54*, 167–173.
61. Ishii, M.; Zuber, N. Drag coefficient and relative velocity in bubbly, droplet or particulate flows. *AIChE J.* **1979**, *25*, 843–855. [CrossRef]
62. Tomiyama, A.; Kataoka, I.; Zun, I.; Sakaguchi, T. Drag coefficients of single bubbles under normal and micro gravity conditions. *JSME Int. J. Ser. B Fluids Therm. Eng.* **1998**, *41*, 472–479. [CrossRef]
63. Besagni, G.; Varallo, N.; Mereu, R. Computational Fluid Dynamics Modelling of Two-Phase Bubble Columns: A Comprehensive Review. *Fluids* **2023**, *8*, 91. [CrossRef]
64. Auton, T.R. The lift force on a spherical body in a rotational flow. *J. Fluid Mech.* **1987**, *183*, 199–218. [CrossRef]
65. Žun, I. The mechanism of bubble non-homogeneous distribution in two-phase shear flow. *Nucl. Eng. Des.* **1990**, *118*, 155–162. [CrossRef]

66. Žun, I. The transverse migration of bubbles influenced by walls in vertical bubbly flow. *Int. J. Multiph. Flow* **1980**, *6*, 583–588. [CrossRef]
67. Ali, M.F.; Gan, J.; Chen, X.; Yu, G.; Zhang, Y.; Ellahi, M.; Abdeltawab, A.A. Hydrodynamic modeling of ionic liquids and conventional amine solvents in bubble column. *Chem. Eng. Res. Des.* **2018**, *129*, 356–375. [CrossRef]
68. Legendre, D.; Magnaudet, J. The lift force on a spherical bubble in a viscous linear shear flow. *J. Fluid Mech.* **1998**, *368*, 81–126. [CrossRef]
69. Drew, D.A.; Lahey, R.T. The virtual mass and lift force on a sphere in rotating and straining inviscid flow. *Int. J. Multiph. Flow* **1987**, *13*, 113–121. [CrossRef]
70. Pourtousi, M.; Sahu, J.N.; Ganesan, P. Effect of interfacial forces and turbulence models on predicting flow pattern inside the bubble column. *Chem. Eng. Process.* **2014**, *75*, 38–47. [CrossRef]
71. Hosokawa, S.; Tomiyama, A.; Misaki, S.; Hamada, T. Lateral Migration of Single Bubbles Due to the Presence of Wall. In Proceedings of the ASME 2002 Joint U.S.-European Fluids Engineering Division Conference, Montreal, QC, Canada, 14–18 July 2002; pp. 855–860.
72. Buwa, V.V.; Ranade, V.V. Dynamics of gas–liquid flow in a rectangular bubble column: Experiments and single/multi-group CFD simulations. *Chem. Eng. Sci.* **2002**, *57*, 4715–4736. [CrossRef]
73. Krishna, R.; Van Baten, J.M.; Ellenberger, J.; Higler, A.P.; Taylor, R. CFD Simulations of Sieve Tray Hydrodynamics. *Chem. Eng. Res. Des.* **1999**, *77*, 639–646. [CrossRef]
74. Wilkinson, P.M. Physical Aspects and Scale-Up of High Pressure Bubble Columns. Ph.D. Thesis, Faculty of Science and Engineering, University of Groningen, Groningen, The Netherlands, 1991.
75. Hughmark, G.A. Holdup and Mass Transfer in Bubble Columns. *Ind. Eng. Chem. Process Des. Dev.* **1967**, *6*, 218–220. [CrossRef]
76. Chen, P.; Sanyal, J.; Dudukovic, M.P. CFD modeling of bubble columns flows: Implementation of population balance. *Chem. Eng. Sci.* **2004**, *59*, 5201–5207. [CrossRef]
77. Möller, F.; Seiler, T.; Lau, Y.M.; Weber, M.; Weber, M.; Hampel, U.; Schubert, M. Performance comparison between different sparger plate orifice patterns: Hydrodynamic investigation using ultrafast X-ray tomography. *Chem. Eng. J.* **2017**, *316*, 857–871. [CrossRef]
78. Kumar, A.; Degaleesan, T.E.; Laddha, G.S.; Hoelscher, H.E. Bubble swarm characteristics in bubble columns. *Can. J. Chem. Eng.* **1976**, *54*, 503–508. [CrossRef]
79. Akita, K.; Yoshida, F. Bubble Size, Interfacial Area, and Liquid-Phase Mass Transfer Coefficient in Bubble Columns. *Ind. Eng. Chem. Process Des. Dev.* **1974**, *13*, 84–91. [CrossRef]


**Disclaimer/Publisher's Note:** The statements, opinions and data contained in all publications are solely those of the individual author(s) and contributor(s) and not of MDPI and/or the editor(s). MDPI and/or the editor(s) disclaim responsibility for any injury to people or property resulting from any ideas, methods, instructions or products referred to in the content.